# Finite-size local dimension as a tool for extracting geometrical properties of attractors of dynamical systems

Martin Bonte[1] and Stéphane Vannitsem[1]

[1]Royal Meteorological Institute of Belgium

**Correspondence:** Martin Bonte (martin.bonte@meteo.be)

**Abstract.** Local dimension computed using Extreme Value Theory (EVT) is usually used as a tool infer dynamical properties of a given state $\zeta$ of the chaotic attractor of the system. The dimension computed in this way is also known as the pointwise dimension in dynamical systems literature, and is defined using a limit for infinitely small neighborhood in the phase space around $\zeta$. Since it is numerically impossible to achieve such limit, and because dynamical systems theory predicts that this

5  local dimension is almost constant over the attractor, understanding the properties of this tool for a finite scale $R$ is crucial. We show that the dimension can considerably depend on $R$, and this view differs from the usual one in geophysics literature, where it is often considered that there is one dimension for a given dynamical state or process. We also systemtically assess the reliability of the computed dimension given the number of points to compute it.

This interpretation of the $R$-dependence of the local dimension is illustrated on the Lorenz 63 system for $\rho = 28$, but also

10  in the intermittent case $\rho = 166.5$. The latter case shows how the dimension can be used to infer some geometrical properties of the attractor in phase space. The Lorenz 96 system with $n = 50$ dimensions is also used as a higher dimension example. A dataset of radar images of precipitation (the RADCLIM dataset) is finally considered, with the goal of relating the computed dimension to the (un)stability of a given rain field.

## 1 Introduction

15  When nowcasting rain field, the future state is essentially predicted using lagrangian persistence (Zawadzki et al. (1994), see Pierce et al. (2012) for a review on nowcasting). It is known that the errors in the estimation of the motion field (the wind) do not dominate the total error of the forecast (Bowler et al., 2007), but that taking into account the growth and dissipation of rain cells is essential for an accurate nowcast (Germann et al., 2006). In the case of convective events, the instability may be captured by the convective available potential energy (CAPE) available in NWP outputs, but convective situations can very quickly evolve.

20  It would therefore be useful to have a real-time method to assess the stability of the current situation. Several techniques have been developed to produce probabilistic forecasts (Germann and Zawadzki, 2004; Bowler et al., 2007; Berenguer et al., 2011; Pulkkinen et al., 2019a). Despite of these, it is still difficult to emit early warnings for very severe floods for example, as witnessed by the 2021 flood in Belgium (Journée et al., 2023).

The idea behind the current work is to use the local dimension of a given state in phase space, as proxy for the complexity

25  (and possibly the predictability) of the future of that state, following Faranda et al. (2017, 2022, 2023); De Luca et al. (2020).

The intuition supporting this idea is that points having a high dimension have a lot of different state space directions in which to evolve, so that their direction of evolution would be more difficult to guess if one had to do it stochastically. Other state space ideas for nowcasting have also been explored in Foresti et al. (2024).

The computation of the dimension of manifolds and attractors of dynamical systems is a huge and old topic (Russell et al. (1980), see Abarbanel (1996); Ott (2002) for textbook reviews in the context of dynamical systems, and Camastra and Staiano (2016) for a review on the dimension in the broader context of manifold dimension estimation). New algorithms were proposed for low dimensional systems and producing mainly global estimation of the dimension: Golay and Kanevski (2014); Erba et al. (2019), see also Bac and Zinovyev (2020). The focus is here on the dimension computed locally in phase space, using the framework of the extreme value theory (EVT), as in proposed in Faranda et al. (2012, 2017, 2019, 2023); Pons et al. (2020, 2023).

The local dimension is also called the pointwise dimension, and its definition is (Ott, 2002)

$$D_p(\zeta) = \lim_{R \to 0} \frac{\ln \mu(B(R))}{\ln R}, \tag{1}$$

where $\mu$ is the natural measure on the attractor and $B(R)$ is the $n$-dimensional ball centered on $\zeta$. This definition implies that $\mu(B(R)) \overset{R \to 0}{\sim} R^{D_p(\zeta)}$ asymptotically (limits of both infinite number of points and infinitely small bulk size). A classical result in dynamical systems theory is that the dimension should asymptotically be the same for all points, $D_p(\zeta) = D_1$ ($D_1$ is the information dimension), except for a zero-measure set of points (Pons et al., 2020; Ott, 2002; Pesin, 1997).

It is obviously impossible to numerically reach the limit $R \to 0$ in (1), and the question is then how to choose some finite value of $R$, as raised for example in Pons et al. (2020). In Datseris et al. (2023), the discussion about the percentage of points needed suggests that $N$ (the number of points at a distance smaller than $R$ from the computation point $\zeta$) just needs to be higher than 100-1000. A similar conclusion is reached in Caby (2019). The idea of evaluating the impact of finite radius $R$ was followed in Little et al. (2017) using a PCA technique in order to identify a scale where the manifold could be approximated by a plane. A similar idea was used to evaluate the robustness to multiscaling of a good estimator in Camastra and Staiano (2016).

In this work, we use a maximum likelihood estimator to estimate the local EVT dimension, for different values of $R$. This estimator turns out to be exactly a local version of the Takens estimator for the global dimension (Takens, 1985). The estimations of the dimension for the different values of $R$ are then used to infer local information on the attractor.

As the focus of the current work is on the non-asymptotic estimation of the dimension, we obviously want to consider only values of the dimension which will not significantly change if more points are added to the dataset: in this sense, we want to be in the limit of infinite number of points. We therefore need some techniques to assess whether the dimension computed for some value of $R$ has sufficiently converged or not.

The main findings of this work are:

1. The non-asymptotic local dimension depends on the scale $R$: this can be used to get information on the phase space structures. This new interpretation of the dimension as dependent on $R$ contrasts with the usual notion of dimension. We illustrate this approach on the Lorenz 63 system for $\rho = 28$ and for $\rho = 166.5$. The latter displays chaotic intermittency (see Sparrow (1982); Ott (2002)), inducing a state space geometry well suited to illustrate our interpretation of the

60     dependence of the dimension on $R$. Another reason to study the behavior of the dimension for intermittent systems, comes from the fact our main goal is to compute the dimension for rain fields, which are known to be intermittent.

2. The question of the number of points $N$ needed to have a robust estimation of the dimension is also explored. The question is raised in Pons et al. (2020) and Datseris et al. (2023) for the EVT dimension. For the correlation dimension (Grassberger and Procaccia, 1983), the definition of the dimension ($size \sim R^{dimension}$) implies, at fixed $R$, that the

65     value of $N$ needed grows exponentially with the dimension (Eckmann and Ruelle, 1992; Camastra and Staiano, 2016).

To clarify this, the normalised root mean squared error (NRMSE) (metric proposed in Datseris et al. (2023)) is used in this work to assess the quality of the fit at a given scale $R$. The confidence bounds provided by the likelihood function are also computed and it is shown the true value of the dimension is around the estimated value with a $10\%$ error and with $95.5\%$ confidence if $N > 427$, seemingly in contradiction with the mentioned argument of Eckmann and Ruelle

70     (1992). We introduce a quantity (denoted $s$ hereafter), which brings some light on this. This gives a possible answer to the question of the maximal dimension that one can measure with the EVT method and in which conditions.

3. The applicability to high-dimensional systems is also explored in the context of the Lorenz 96 with $n = 50$ dimensions, for which the dependence of the dimension on $R$ gives some characterization of the phase space.

Radar-estimated rain field over Belgium is investigated with the same tools. In this case, the dimensions for some com-

75     putation points $\zeta$ can be reliably estimated, but only for very narrow ranges of $R$, and this makes it difficult to draw conclusions on the dynamical properties of the state based on the values of the dimension. The dimension ranges essentially between 10 and 30, with a lot of values between 15 and 20. Not surprisingly, we also find a correlation between the convective rain rate from ERA5 reanalysis and the relevant range of values of $R$.

This paper is organized as follows. In section 2, we first introduce the pointwise dimension and show how it is computed in

80  the EVT framework. We also derive the maximum likelihood estimator of the dimension and the expressions for the bounds of the confidence interval using the likelihood function. After that, we introduce the NRMSE score and interpret the estimated dimension. We also introduce the quantity $s$ in order to understand the maximum dimension that one can compute using a given number of points.

Section 3 introduces the results of the computed dimension on the Lorenz 63 system (for $\rho = 28$ and $\rho = 166.5$) and discuss

85  in details the interpretation. The intermittent case illustrates well that the dimension depends on the radius $R$, and can be used as a tool to evaluate the geometric properties of the attractor, such as the distance of chaotic points to the laminar regime.

Large systems (Lorenz 96 with $n = 50$ dimensions and the radar dataset) are considered in Section 4 and the last section briefly summarizes the work.

## 2 Framework for the estimation of the dimension

The pointwise dimension for a computation point $\zeta$ is defined in terms of the natural measure $\mu$ on the attractor by (1):

$$D_p(\zeta) = \lim_{R \to 0} \frac{\ln C(R)}{\ln R}. \tag{2}$$

This is equivalent to

$$\mu(B(R)) \overset{R \to 0}{\sim} R^{D_p(\zeta)} \tag{3}$$

i.e. the measure of the ball $B(R)$ of radius $R$ around $\zeta$ scales as $R^{D_p(\zeta)}$. In the limit of infinite trajectories, this measure can be approximated as the number $C(R)$ of points inside $B(R)$, divided by the total number of points in the trajectory. In other words, the pointwise dimension $D_p(\zeta)$ can thus be interpreted as a characterization of the growth rate of the number of points that one should find inside a ball $B(R)$ centered around $\zeta$ (for infinitely small $R$).

If there are enough points around $\zeta$, and if they form a smooth $D_p(\zeta)$-dimensional surface, one can introduce the hyperspherical coordinates $(r, \boldsymbol{\theta})$ and the density of points $\sigma(r, \boldsymbol{\theta})$. In this case,

$$C(R) = \int_0^R dr \, r^{D_p(\zeta)-1} \Sigma(r) \tag{4}$$

with $\Sigma(r) = \int d\boldsymbol{\theta}\sigma(r, \boldsymbol{\theta})$ being the density integrated over angles. The correlation integral $C(R)$ is proportional to $R^{D_p(\zeta)}$ if and only if $\Sigma(r)$ is constant. If not, one has to consider the small $R$ limit, where $C$ can be expanded in Taylor series. One can check that the first nonzero term of this series is the one of order $D_p(\zeta)$ (from now, we use the notation $\delta = D_p(\zeta)$):

$$C(R) = C^{(\delta)}(0)\frac{R^\delta}{\delta!} + O(R^{\delta+1}). \tag{5}$$

For example, for $\delta = 2$, we have

$$C(0) = 0 \tag{6}$$

$$C'(0) = R\Sigma(R)|_{R=0} = 0 \tag{7}$$

$$C''(0) = (R\Sigma(R))'|_{R=0} = \Sigma(0), \tag{8}$$

so that $C(R) = \frac{R^2}{2}\Sigma(0) + O(R^3)$. This approximation amounts to consider $\Sigma$ constant on the interval of integration $[0, R]$ because the term containing $\Sigma'(0)$ is neglected.

After estimation of $C(R)$ for several values of $R$, and if it has the expected scaling $C(R) \sim R^\delta$, the dimension can be extracted using a fit on this scaling. In the context of the correlation dimension, $C(R)$ is a local version of the correlation integral and $\delta$ can be computed as $\frac{\ln C(R_2) - \ln C(R_1)}{\ln R_2 - \ln R_1}$ ($R_1$ and $R_2$ have to be chosen).

Whatever technique we use to estimate $\delta$, the following points have to be kept in mind:

– The distances measured in phase space do not precisely match with $r$ or $R$: if the surface is curved, the points on the boundary of $B(R)$ will have a distance along the surface of the attractor bigger than $R$ (see Fig. 1). Therefore, the
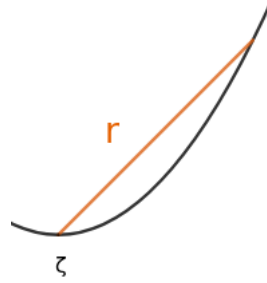
**Figure 1.** Illustration that the distance computed in phase space might be different than the distance on the surface: the distance $r$ computed in phase space is in red, while $r$ should be measured along the surface of which we are trying to estimate the dimension (which is in black), in order to find the $C(R) \sim R^\delta$ behavior.

number of points in $B(R)$ might not scale exactly as $R^\delta$. This could lead to a bias in the estimated dimension (Perinelli et al., 2023). Since the distance computed in phase space becomes closer to the one computed on the surface when $R$ is small enough (i.e. smaller than some typical scale of the curvature), $C(R)$ will have the correct behaviour in that limit.

– If we use a too big value of $R$, the $R^{\delta+1}$ term in (5) might not be small anymore. Said differently, $\Sigma(r)$ in (4) is not sufficiently constant on $[0, R]$ for $C(R) \sim R^\delta$ to hold. Actually, if in this range, $\Sigma(r)$ looks more like $\sim r^a$ for $a \neq 0$, $C(R)$ will scale as $R^{\delta+a}$. The value of the dimension we will measure in this case does not have a clear geometric meaning, but is an effective value $\delta_{eff} = \delta + a$, taking into account the change of $\Sigma$ over $[0, R]$.

In this case, the information contained in $\delta_{eff}$ is much more difficult to use. If one had a way to estimate $a$ in $\Sigma(r) \sim r^a$, one could compute $\delta = \delta_{eff} - a$.

## 2.1 Dimension and extreme value theory

Extreme value theory is a framework to study the occurences of extreme events (see for example the textbooks (Beirlant et al., 2004; Falk et al., 2010; Lucarini et al., 2016)).

Two approaches can be followed to define extremes among samples $\{X_i\}_{i=1,\dots n}$. The Peak Over Threshold (POT) consists in fixing a threshold $u$, and values $X_i > u$ above this threshold are considered as extremes. The threshold $u$ has to be taken as high as possible to reach the correct definition of extremes. The Block Maxima (BM) approach consists in splitting the set of samples in chunks of size $m$, and the extremes are the highest values of each chunk (one extreme for each chunk). The size $m$ has to go to infinity in order to correctly define of extremes.

The main theorem in the BM approach states under some conditions, that there are essentially three asymptotic distribution for extremes, regrouped under the Generalized Extreme Value (GEV) law. In the POT approach, an equivalent theorem states

that the limiting distribution is a Generalised Pareto Distribution (GPD):

$$GPD_\xi(z) = \begin{cases} (1+\xi z)^{-1-1/\xi} & \text{for } \xi \neq 0 \\ e^{-z} & \text{for } \xi = 0 \end{cases} \tag{9}$$

where the support of $z$ is $z \geq 0$ for $\xi \geq 0$ and $0 \leq z \leq -1/\xi$ for $\xi < 0$.

### 2.1.1 Theoretical extreme value law around $\zeta$

140  The scaling $C(R) \sim R^\delta$ is the starting point to estimate the dimension in the EVT framework using the POT approach (Faranda et al., 2012). We reformulate here some of their results.

Consider the ball $B(R)$ of radius $R$ in the $n$-dimensional phase space. $C(R) \sim R^\delta$ implies that the number of points between $r$ and $r + dr$ is

$$c(r)dr \sim C'(r)dr \sim \delta\, r^{\delta-1}\, dr. \tag{10}$$

145  In order to have a pdf between 0 and $R$ (i.e. in the $B(R)$ ball), $c$ is normalized to 1 ($\int_0^R c(r)dr = 1$), so that

$$c(r) = \frac{\delta\, r^{\delta-1}}{R^\delta} \tag{11}$$

The usual EVT framework for the dimension is found by using one the following transformations:

$$g_1(r) = -\ln r, \quad g_2(r) = r^{-1/\alpha}, \quad g_3(r) = K - r^{1/\gamma}. \tag{12}$$

The parameter $K$ can be freely chosen, and $\alpha$ and $\gamma$ have to be positive. Using these transformations and their inverses, the
150  pdf's describing the distributions of $g_a = g_a(r)$ ($T_a = g_a(R)$ and $g_a > T_a$) are written as

$$f_{1,T_1}(g_1) = \delta e^{-\delta(g_1-T_1)}, \quad f_{2,T_2}(g_2) = \frac{\delta\alpha}{T_2}\left(\frac{g_2}{T_2}\right)^{-\delta\alpha-1}, \quad f_{3,T_3}(g_3) = \frac{\delta\gamma}{D-T_3}\left(\frac{K-g_3}{K-T_3}\right)^{\delta\gamma-1}, \tag{13}$$

and one can check that each of these distributions correspond exactly to one of the signs of $\xi$ ($\xi = 0$, $\xi > 0$ and $\xi < 0$) of the GPD (9), with

$$
\begin{aligned}
f_{1,T_1}(g_1)dg_1 &= GPD_0(z)dz && \text{with } z = \delta(g_1 - T_1) \\
f_{2,T_2}(g_2)dg_2 &= GPD_\xi(z)dz && \text{with } \xi = \tfrac{1}{\delta\alpha} \text{ and } \tfrac{g_2}{T_2} = 1 + \xi z \\
f_{3,T_3}(g_3)dg_3 &= GPD_\xi(z)dz && \text{with } \xi = -\tfrac{1}{\delta\gamma} \text{ and } \tfrac{K-g_3}{K-T_3} = 1 + \xi z
\end{aligned}
\tag{14}
$$

155  Note that, starting from one of the three possible distributions in (14) and using the corresponding transformations (12), one recovers back equation (11). That is, the application of each one of the transformations in (12) and the deduction of $\delta$ using a parameter fit of the corresponding distribution in (14), is an alternative way to access the exponent $\delta$ of the scaling $C(R) \sim R^\delta$.

If we choose $\gamma = 1$ and $D = 0$ in the third case, $f_{3,T_3}(g_3)dg_3$ is exactly equal to (11), which is actually already in an EVT form.

### 2.1.2 Maximum likelihood estimation of $\delta$

Let us now derive the expression of the maximum likelihood (ML) estimator of the dimension, using the above density functions. It in fact leads to the expression of a local version of the estimator of Takens (Takens, 1985).

To compute the dimension around a computation point $\zeta$, consider all points inside the ball $B(R)$ centered on $\zeta$ ("the analogues"), whose distances to $\zeta$ are $r_i$ (with $i = 1, \ldots, N$ and $r_i < R$). The corresponding $g$'s are defined as $g_{a,i} = g_a(r_i)$. We know from the previous section that the $g_{a,i}$'s should follow the distribution $f_{a,T_a}$.

The (log)-likelihood functions are:

$$L_1 = \prod_{i=1}^{N} \delta e^{-\delta(g_{1,i}-T_1)}, \quad \ln L_1 = N \ln \delta - \delta \sum_{i=1}^{N}(g_{1,i}-T_1) \tag{15}$$

$$L_2 = \prod_{i=1}^{N} \delta\alpha \left(\frac{g_{2,i}}{T_2}\right)^{-\delta\alpha-1}, \quad \ln L_2 = N \ln(\delta\alpha) - (\delta\alpha+1) \sum_{i=1}^{N} \ln\left(\frac{g_{2,i}}{T_2}\right) \tag{16}$$

$$L_3 = \prod_{i=1}^{N} \delta\gamma \left(\frac{K-g_{3,i}}{K-T_3}\right)^{\delta\gamma-1}, \quad \ln L_3 = N \ln(\delta\gamma) + (\delta\gamma-1) \sum_{i=1}^{N} \ln\left(\frac{K-g_{3,i}}{K-T_3}\right) \tag{17}$$

Setting the derivative of $\ln L$ with respect to $\delta$ to 0 in each case gives the ML estimator:

$$\frac{1}{\hat{\delta}_1} = \frac{\sum_{i=1}^{N}(g_{1,i}-T_1)}{N}, \quad \frac{1}{\hat{\delta}_2} = \frac{\alpha}{N} \sum_{i=1}^{N} \ln\left(\frac{g_{2,i}}{T_2}\right), \quad \frac{1}{\hat{\delta}_3} = -\frac{\gamma}{N} \sum_{i=1}^{N} \ln\left(\frac{D-g_{3,i}}{D-T_3}\right) \tag{18}$$

These three estimators are numerically equal. Indeed, using $g_{1,i} = -\ln r_i$, $g_{2,i} = r_i^{-1/\alpha}$ and $g_{3,i} = K - r_i^{1/\gamma}$, one has

$$\frac{1}{\hat{\delta}_1} = \frac{1}{N} \sum_i (-\ln r_i + \ln R) = -\frac{1}{N} \sum_i \ln \frac{r_i}{R} \tag{19}$$

$$\frac{1}{\hat{\delta}_2} = \frac{\alpha}{N} \sum_i \ln\left(\frac{r_i}{R}\right)^{-1/\alpha} = -\frac{1}{N} \sum_i \ln \frac{r_i}{R} \tag{20}$$

$$\frac{1}{\hat{\delta}_3} = -\frac{\gamma}{N} \sum_i \ln\left(\frac{r_i}{R}\right)^{1/\gamma} = -\frac{1}{N} \sum_i \ln \frac{r_i}{R} \tag{21}$$

The estimated inverse dimensions $1/\hat{\delta}_a$ are all equal to

$$\frac{1}{\hat{\delta}_a} = -\frac{1}{N} \sum_i^N \ln \frac{r_i}{R} = -\ln \operatorname{geom}\left(\frac{r_1}{R}, \ldots, \frac{r_N}{R}\right) \tag{22}$$

which is minus the mean of $\frac{r_i}{R}$ in logarithmic scale, or minus the logarithm of the geometric mean of the ratios $\frac{r_i}{R}$. This is precisely a local version of the expression of the estimator of the local dimension as given by Takens (Takens, 1985).

This ML estimator is particularly interesting in this case since it is, even for finite $N$, unbiased and efficient as estimator (James, 2006).

These three different ML principles are really equivalent since the loglikelihood functions are all equal up to a term independent of $\delta$ (so that the derivatives of the loglikelihood functions are equal). Indeed, using the different but equal expressions

of $\hat{\delta}$ in terms of the $g_{a,i}$'s, one has

$$\ln L_1(\delta) = N \ln \delta - \delta \sum_i (g_{1,i} - T) = N \ln \delta - N \delta \hat{\delta}^{-1} \tag{23}$$

$$\ln L_2(\delta) = N \ln(\delta\alpha) - (\delta\alpha + 1) \sum_i \ln \frac{g_{2,i}}{T_2} = N \ln(\delta\alpha) - (\delta\alpha + 1) \frac{N}{\hat{\delta}\alpha} = \ln L_1(\delta) + N \ln \alpha - \frac{N}{\hat{\delta}\alpha} \tag{24}$$

$$\ln L_3(\delta) = N \ln(\delta\gamma) + (\delta\gamma - 1) \sum_i \ln \left( \frac{K - g_{3,i}}{K - T_3} \right) = N \ln(\delta\gamma) - (\delta\gamma - 1) \frac{N}{\hat{\delta}\gamma} = \ln L_1(\delta) + N \ln \gamma + \frac{N}{\hat{\delta}\gamma}. \tag{25}$$

The three different loglikelihood functions are thus equal, up to an additive term independent of $\delta$.

In Pons et al. (2023), the authors also estimate the shape parameter ($\xi$) of the observed extreme value law of the $g_{a,i}$'s. We do not do it since it is the choice of the function $g_a(r)$ which fixes the extreme value law to expect. If there is a deviation from this law, it is because the scaling $C(R) \sim R^\delta$ is not satisfied in the first place (see section 2.5 for possible reasons why $C(R) \sim R^\delta$ does not hold).

### 2.1.3 Confidence intervals

Confidence bounds on the estimations of the dimension were already studied to some extent in Theiler (1990), but through the statistical error on the estimation of $C(R)$. Since we do not rely on estimations of $C(R)$ and use only a ML principle for $\hat{\delta}$, we present here the computation of the bounds of the confidence intervals of $\delta$ using the likelihood function.

The loglikelihood function in the first case ($g_1(r) = -\ln r$) is

$$\ln L_1(\delta) = N \ln \delta - N \delta \hat{\delta}^{-1} \tag{26}$$

and $\ln L_2$ and $\ln L_3$ are the same functions of $\delta$, up to an irrelevant term, as shown in section 2.1.2. We have thus

$$\Delta \ln L_1(\delta) = \Delta \ln L_2(\delta) = \Delta \ln L_3(\delta) \tag{27}$$

where $\Delta \ln L_a(\delta) = \ln L_a(\delta) - \ln L_a(\hat{\delta})$. Since the computation of confidence bounds using the likelihood involves only $\Delta \ln L$, the confidence bounds will be the same for all three cases.

One can have a $n_\sigma$ confidence interval by finding the values of $\delta$ for which (James, 2006)

$$\Delta \ln L(\delta) = N \left( \ln \frac{\delta}{\hat{\delta}} - \frac{\delta}{\hat{\delta}} + 1 \right) = -\frac{n_\sigma^2}{2} \tag{28}$$
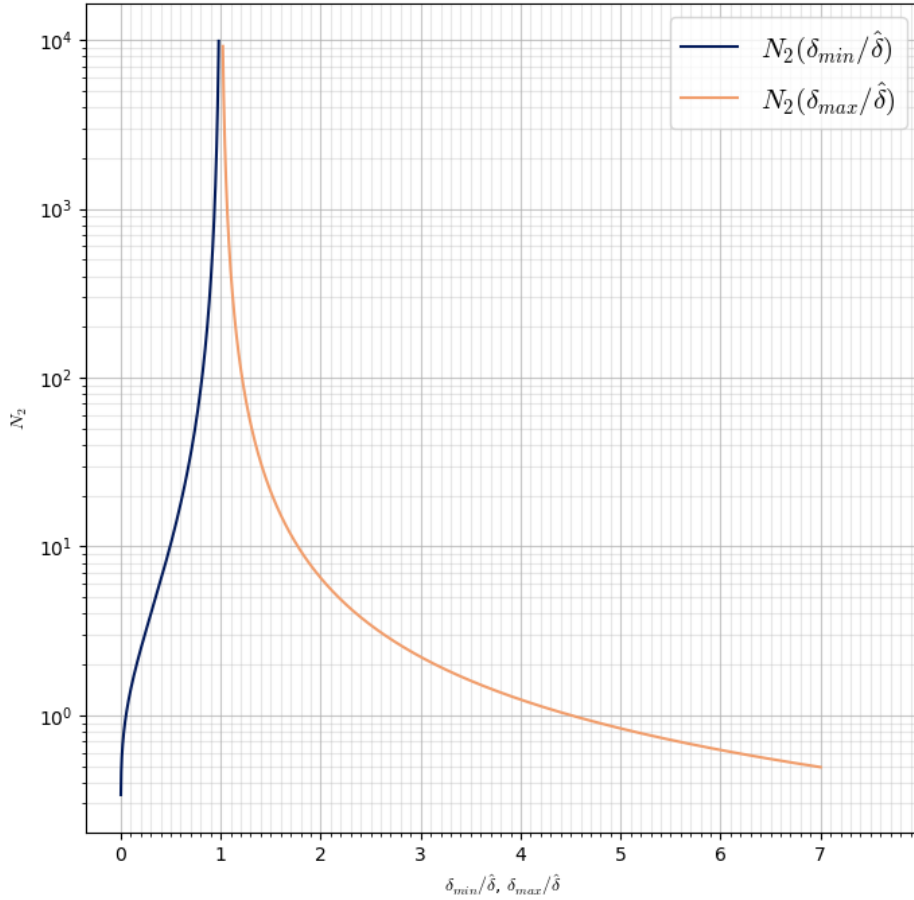
If we fix some target confidence interval $[\delta_{min}, \delta_{max}]$ around $\hat{\delta}$, one should thus use

$$N \geq \max \left[ N_{n_\sigma} \left( \frac{\delta_{min}}{\hat{\delta}} \right), N_{n_\sigma} \left( \frac{\delta_{max}}{\hat{\delta}} \right) \right], \quad N_{n_\sigma} \left( \frac{\delta}{\hat{\delta}} \right) = -\frac{n_\sigma^2}{2} \left( \ln \frac{\delta}{\hat{\delta}} - \frac{\delta}{\hat{\delta}} + 1 \right)^{-1} \tag{29}$$

For example, if we want a 10% interval (i.e. $\delta_{min} = 0.9\hat{\delta}$ and $\delta_{max} = 1.1\hat{\delta}$) with 95.5% confidence ($n_\sigma = 2$), the required $N$ is computed as

$$N \geq \max(N_2(0.9), N_2(1.1)) = \max(373.1, 426.5) = 426.5. \tag{30}$$

**8**

**Figure 2.** Plot of $N_2$ versus of $\frac{\delta_{min}}{\hat{\delta}}$ and $\frac{\delta_{max}}{\hat{\delta}}$ ($n_\sigma = 2$, $95.5\%$ confidence).

210 So $N$ has to be bigger than 427 to be sure at $95.5\%$ that the true dimension is $10\%$ below or $10\%$ higher than $\hat{\delta}$.

Figure 2 shows a plot of the functions $N_2\left(\frac{\delta_{min}}{\hat{\delta}}\right)$ and $N_2\left(\frac{\delta_{max}}{\hat{\delta}}\right)$.

One can also invert the relation to compute $\frac{\delta}{\hat{\delta}}$ in terms of $N$:

$$\frac{\delta_{min}}{\hat{\delta}} = -W_0(-e^{-a}) \tag{31}$$

$$\frac{\delta_{max}}{\hat{\delta}} = -W_{-1}(-e^{-a}) \tag{32}$$

215 where $W_0$ and $W_{-1}$ are the Lambert function or order $0$ and $-1$ respectively, and $a = \frac{n_\sigma^2}{2N} + 1$. Note that these relative bounds depend only on the number of observations, i.e. on the number of analogues, and not on the dimension itself!

These bounds should be taken with caution. They are computed supposing that the underlying distribution of points is indeed exponential and that all the samples are IID, as was already pointed out in Theiler (1990). In the case of a dynamical system producing the dataset, this is only true in the asymptotic limit. Consider for example a system observed with very high time

220   resolution but on a quite short time. In this case, the system could have visited only a few times the ball $B(R)$ (so that the

system has not explored all directions around $\zeta$ yet) but one could still have $N \geq 427$. In such case, the distribution of values

of $r$ around $\zeta$ has not converged yet and we cannot really trust the confidence interval $0.9\hat{\delta} \leq \delta \leq 1.1\hat{\delta}$. It is however unlikely

that the observed distribution of values of $r$ looks like an exponential. The NRMSE score introduced below helps to quantify

how the experimental distribution is far from an exponential distribution.

225   **2.2   NRMSE score**

The ML method produces an estimate of the dimension even if the distribution of points is not at all an exponential, in which

case the estimated dimension and its bounds are not correct. A systematic way to assess whether the fitted distribution is indeed

exponential or not is therefore needed.

As in Datseris et al. (2023), we tried to use a Kolmogorov-Smirnov test but it did not prove to be very efficient to assess the

230   quality of the exponential fit to the data. Following their suggestion, the normalised root mean squared error (NRMSE) is used

instead between the fitted version of the exponential distribution $f_{1,T_1}$ and a uniform distribution. It is computed as follows:

1. the data are first binned in bins of equal size and the empirical probability $P_i$ associated with bin $i$ is computed as the
   fraction of observations lying in bin $i$ (the number of bins is taken as the minimum between the Sturge's rule and the
   Freedman-Diaconis rule, see Scott (2015) about those rules);

235   2. the $E_i$'s are defined as the fraction of events that would fall into each of the bins, if the events follow an exponential law
   characterized by $\hat{\delta}$;

3. $U$ is defined as the probability of falling into each bin using a uniform law over the range of observations;

4. the NRMSE score is then computed as

$$\text{NRMSE} = \sqrt{\frac{\sum_i (P_i - E_i)^2}{\sum_i (P_i - U)^2}} \tag{33}$$

240   The NRMSE score gives an indication of how much the data is better described by an exponential law than by a uniform law. For

a good fit, we expect a small NRMSE score: in this case, the numerator (which is the error between the experimental distribution

and the fitted exponential distribution) is much lower than the denominator (which is the error between the experimental

distribution and the uniform distribution).

**2.3   Interpretation of the estimated dimension**

245   The interpretation of the dimension is more easily understandable in the third case, with $g_3(x) = -x$ (with $\gamma = 1$). Since the

values of $\delta$ obtained in each case are equal, the interpretation holds irrespectively of the function $g_a$ used.

Figure 3 shows two possible histograms for two random variables following both the distribution $f_{3,T_3} = \left(\frac{g_3}{T_3}\right)^{\delta-1} = $

$\left(\frac{r}{R}\right)^{\delta-1}$ (i.e. with $D = 0$ and $\gamma = 1$), but for two different values of $\delta$. If the empirical distribution of radii $r_i$ (normalized
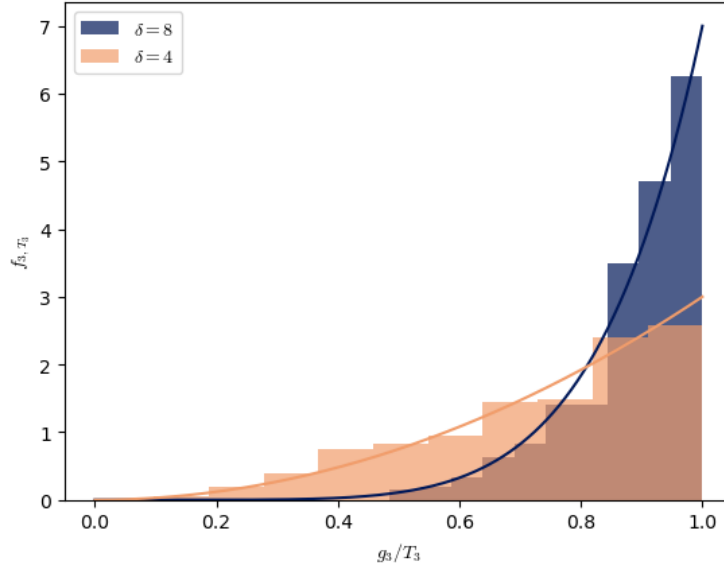
**Figure 3.** Example of histograms of two random variables $g_3 = -r$, whose PDFs for both are $f_{3,T_3} = \left(\frac{g_3}{T_3}\right)^{\delta-1} = \left(\frac{r}{R}\right)^{\delta-1}$ (i.e. with $D = 0$ and $\gamma = 1$), but for different values of $\delta$. The horizontal axis is $\frac{g_3}{T_3} = \frac{r}{R}$.

by $R$) looks like that of the orange histogram, the estimated value $\hat{\delta}$ will be lower than if the empirical distribution is closer
250  to the dark blue histogram. Mathematically, this is because the higher the value of $\delta$, the steeper $r^{\delta-1}$ is. This means that, the higher the dimension, the more the analogues inside $B(R)$ will be close to the boundary of $B(R)$. In the following the estimated value of the dimension can be artificially high because of that.

### 2.4   Measure a high dimension with a small $N$?

The computation of Section 2.1.3 indicates that with $N \gtrsim 400$ (and if the NRMSE score is good), a $10\%$ accuracy is reached
255  for the estimation of $\delta$, for all values of the dimension. This seems in contradiction with the the argument of Eckmann and Ruelle (1992) (i.e. the number of points in $B(R)$ should be an exponential of $\delta$). In this section, we examine in detail how the scaling $C(R) \sim R^\delta$ is consistent with the computation in 2.1.3.

If we denote $\ln \frac{R}{r_i} = g_{1,i} - T_1$ as $x_i$, the computation of section 2.1.1 implies that the $x_i$'s follow an exponential law $f_1(x) = \delta e^{-\delta x}$. In terms of this exponential distribution, $\delta^{-1}$ is interpreted as the scale (see Fig. 4). The ML estimator of the scale of an
260  exponential is the mean of the $x_i$'s, so that we recover the expression $\hat{\delta}^{-1} = \frac{1}{N} \sum_i x_i$ from the section 2.1.2. From this point of view, a large dimension just means a smaller scale for the exponential, which is why it is not much more difficult to measure.

If we denote by $r_0$ the smallest of the $r_i$'s and by $x_0 = \ln \frac{R}{r_0}$ the biggest of the $x_i$'s, one has obviously $\delta^{-1} < x_0$. If there are enough points to estimate $\delta^{-1}$, $x_0$ must be quite far to the right of the plot in Fig. 4, so that a necessary condition is $\delta^{-1} \ll x_0$,
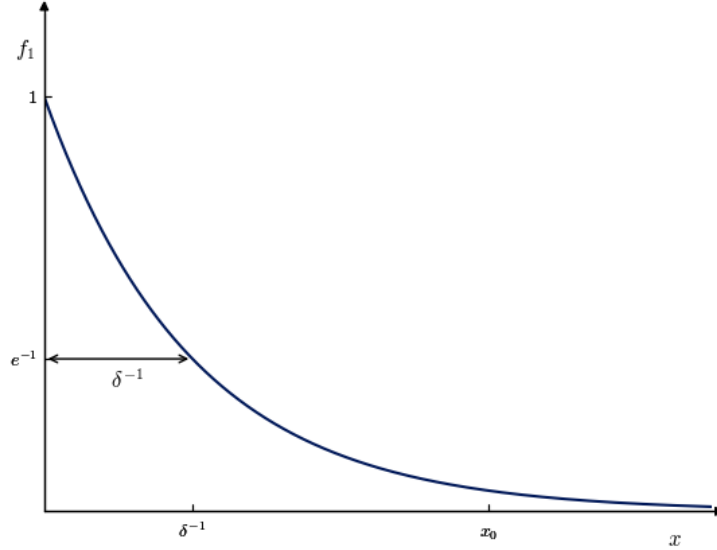
**Figure 4.** An exponential distribution and its scale parametrized by $\delta^{-1}$.

or

$$s \gg 1, \quad s \equiv x_0 \, \delta \tag{34}$$

This expresses that $x_0$ has to be large with respect to the scale $\delta^{-1}$ of the exponential. Conversely, if $s \gg 1$, this means that the exponential has been sampled enough to get a high value for $x$ (namely $x_0$).

One could think that the condition (34) is actually easier to fulfill if the scale $\delta^{-1}$ is smaller (and the dimension bigger), because this leaves "more room" for $x_0$. But this is not the case, since a smaller scale means that the exponential will be more peaked near $x = 0$ (which represents $r = R$), so it will be more difficult to have a sample $x$ with a high value. This is consistent with the fact that the number $N = C(R)$ of points inside $B(R)$ satisfies

$$\frac{R}{r_0} = N^{1/\delta}, \tag{35}$$

(using the scaling $C(R) \sim R^\delta$ and the fact that $C(r_0) = 1$ since $r_0$ is the smallest of the $r_i$'s). This equality shows that, for a fixed $N$, the ratio over which the scaling (3) holds quickly approaches 1. This is the price to pay to measure high dimensions with a reduced number of points, and this poses some difficulties when dealing with large systems (see section 4).

Some remarks:

– Using (35), one can see that $s$ should be just $\ln N$ and the condition (34) is simply

$$\ln N \gg 1. \tag{36}$$

In practice, the distributions are exactly exponential only in the limit $R \to 0$, so that $s$ and $\ln N$ are not exactly equal.

280     – This equivalence between the estimation of different dimensions is because of the scaling transformation of the exponential distribution $f_1$:

$$
\begin{cases}
x & \rightarrow & \lambda x \\
\delta & \rightarrow & \frac{\delta}{\lambda}
\end{cases}
\quad , \quad
f_1(x) = \delta e^{-\delta x} \rightarrow \frac{1}{\lambda} f_1(x)
\tag{37}
$$

which makes the values of the dimension somewhat equivalent to measure. Again, in terms of an exponential distribution, the dimension is just the inverse of the scale of the exponential. The probability density functions $f_{2,T_2}$ and $f_{3,T_3}$, and

285     adapted definitions of $x$ in each cases, have similar scaling properties. These make possible to absorb a redefinition of $\delta$ in a redefinition of $x$ if one uses $f_{2,T_2}$ or $f_{3,T_3}$ instead of $f_{1,T_1}$.

– If the EVT estimator for $\delta$ is able to produce a high value over some range, the estimation of the dimension through the correlation dimension can also do it. Indeed, in both cases, $\hat{\delta}$ is obtained by somehow fitting the scaling $C(R) \sim R^\delta$. The limitation for the correlation dimension is the same than for the EVT dimension: when $\delta$ increases, the range over which

290     this scaling can hold decreases.

The left panel of Fig. 5 shows a scatter plot of $\ln N$ against $s$, with the color being the NRMSE score for dimensions in the Lorenz 63 system (see Appendix A about the Lorenz 63 system). Each point in both panels of Fig. 5 represents a fit. We computed the dimension for 1000 points, for 20 percentages, so there are 20 000 points in each scatter plot of this Figure. A given computation point $\zeta$ in the phase space is therefore represented several times. Here and in the following, we estimated $s$

295     as $s = x_0 \hat{\delta}$.

The right panel of Fig. 5 shows a scatter plot between the NRMSE score and $s$ for the Lorenz 63 system. The form of this plot is quite characteristic and will be encountered several times in the paper. The NRMSE score clearly decreases as $s$ increases: this part corresponds to fits increasingly better. When $s > 10$, the NRMSE reaches a plateau. The NRMSE for some high values of $s$ and $N$ is not so good, this is when the $B(R)$ ball is too big and the distribution in it cannot be a power law

300     (see section 3.2). In practice, one finds that $s$ bigger than $4 - 5$ seems to give NRMSE scores below $0.4$ and these values be used to keep the reliable fits.

In summary, the section 2.1.3 has shown that, for a given relative accuracy, all dimensions require the same number of points inside $B(R)$. This might seem surprising because of the scaling $C(R) \sim R^\delta$, but can actually be understood if we see $\delta^{-1}$ as the scale of the exponential distribution of the $g_1$'s. However, the range of values of $R$ over which the dimension can be

305     measured decreases with the dimension. This is why there is no contradiction with the original argument of Eckmann and Ruelle (1992), which supposed that $R$ is fixed.

In the following analyses, we use scatter plots in the form of that of the right panel of Fig. 5. The rough agreement between $s$ and $\ln N$ can be seen as a consistencty check that the distributions of values of $g_{1,i}$ are indeed close to exponentials (and equivalently, that the distributions of $r_i$ are close to power laws).
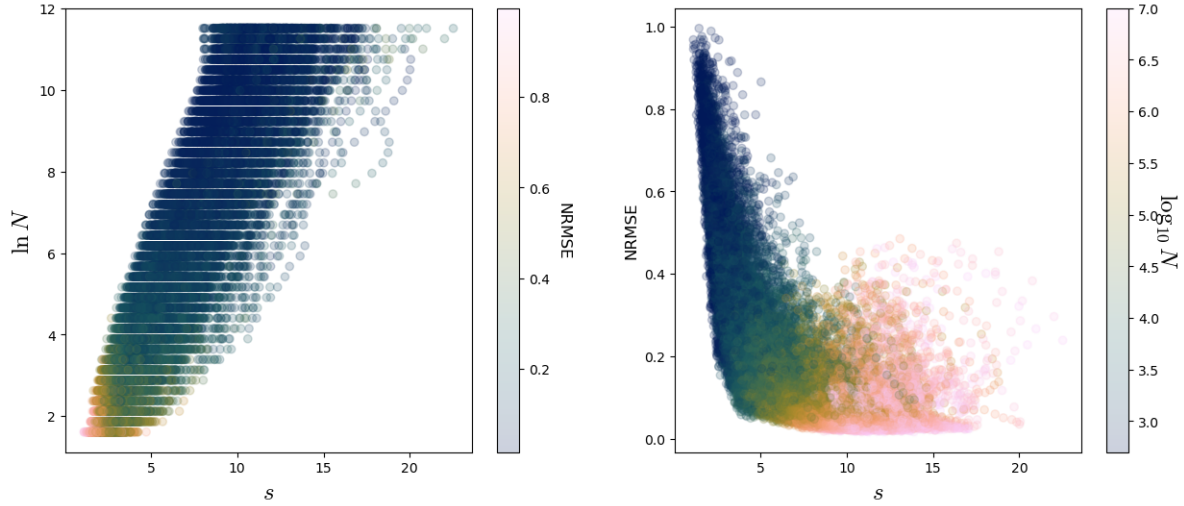
**Figure 5.** For the Lorenz 63 system (see Appendix A) with $\rho = 28$, $10^6$ points. Left: scatter plot of $\ln N$ against $s$. The color is the NRMSE of the fit. Right : scatter plot of the NRMSE against $s$. The color is the $10-$logarithm of the number of points used in the exponential fit. There are 1000 points and 20 fits for each.

## 2.5 Possible phenomena affecting the value of the dimension

The last sections develop tools to quantify how good is a fit to the exponential law. However, different phenomena can affect $\hat{\delta}$ for a given $R$.

If the NRMSE or $s$ do not have good scores, the points in $B(R)$ do not follow a $R^\delta$ law. The cause of this could be one of the following:

1. there are not enough points inside $B(R)$ to properly recognise an exponential (and make the difference with a uniform law)

2. the points are not statistically independent. This was already noted in Theiler (1990)

3. $R$ is too big. To observe the $C(R) \sim R^\delta$ law, one indeed needs to consider a flat neighborhood around $\zeta$ and, if $R$ is too large, this law could be affected by the curvature (Perinelli et al., 2023), or by another geometric feature entering $B(R)$.

On the other hand, if the NRMSE and $s$ give good scores, this means that the number of points inside $B(R)$ indeed follows a power law $R^{\hat{\delta}}$. This could have different causes and a non-exhaustive list is:

1. the estimated value of the dimension can indeed reflect the dimension of the surface supporting the neighbouring points. This happens if the density of points is constant and the "surface" is approximately flat.

2. if there is a clear structure of points in the phase space, with a the density of points of this structure being higher enough than its surroundings, the estimated dimension $\hat{\delta}$ will be that of this structure. This is because the intersection of such

**14**

a structure with the ball $B(R)$ will make the number of points scale as $R^\delta$, where $\delta$ is the dimension of the structure. Such a situation is shown schematically in Fig. 6: in a plane, there is a straight line crossing $B(R)$ and the density $\lambda$ of points on that line is much higher than anywhere else in $B(R)$. The number of points in $B(R)$ will then be essentially the number of points on that line. A simple computation gives $C(R) = 2\lambda\sqrt{R^2 - a^2}$, and if $a \ll R$ (i.e. if $\zeta$ is close enough to the line), $C(R) \approx 2\lambda R$. The scaling of $C(R)$ around $\zeta$ becomes that of the line, even though $\zeta$ is not strictly on it.

The previous case and this one are cases where the estimated dimension is the dimension of some geometric structure in the phase space. This geometric dimension is only well-defined in ranges of $R$ where the geometry is homogeneous in this range: if at a given $R$, the curvature changes or a different geometric feature enters $B(R)$, one can not give a geometric meaning to the dimension. It is only for the values of $R$ for which there are clear objects that the dimension can be interpreted geometrically. In particular, one can approach the dimension in the limit $R \to 0$ only when $R$ is below any other geometric scale. This will be illustrated in the next sections.

Note that this kind of geometric dimension is conceptually equivalent to the one measured by local PCA techniques (such as in Little et al. (2017)).

3. the fact that $C(R) \sim R^\delta$ supposes that the density of points is uniform in the range over which the estimation is done. If the density is increasing when getting away from $\zeta$ (i.e. for increasing $r$, $\Sigma \sim r^a$ for $a > 0$), the empirical histogram of the values of $r$ will be inflated for values of $r$ close to $R$. In that case, the estimated distribution will be closer to the dark blue curve than to the orange curve in Fig. 3, so that the estimated dimension will be higher than the dimension of the surface supporting the points (the "geometric dimension"). In the same way, if the density of points decreases, the estimated dimension will be lower (see remarks in section 2).

In practice, it is not likely that the density $\Sigma$ will follow the same behavior $\Sigma \sim r^a$ on a long range of values of $r$, and one can try to identify when this happens because the dimension will be fluctuating over the range.

Unfortunately, the tools we developed (the NRMSE and the quantity $s$) can give good scores in all three cases and do not allow to make the difference between each of these cases. One has therefore to keep in mind all possible phenomena affecting the estimation of the dimension, and inspect the values of the dimension over some range of values of $R$, in order to interpret the geometry of the system in this range.

In the following, as is usual when computing dimension from time series, a Theiler window around each computation point $\zeta$ was applied (Theiler, 1986), in order to avoid having points to close in time inside the ball $B(R)$.

## 3 Application to small systems

To illustrate some aspects described in the previous sections, we compute the local dimension for small systems, allowing to get some insight of what is captured by the estimated dimension.

The classical Lorenz 63 system for $\rho = 28$ (Lorenz, 1963) is first considered. The relatively simple geometry allows to illustrate some of the phenomena described in Section 2.5. We then present the results of the computation of the local dimension
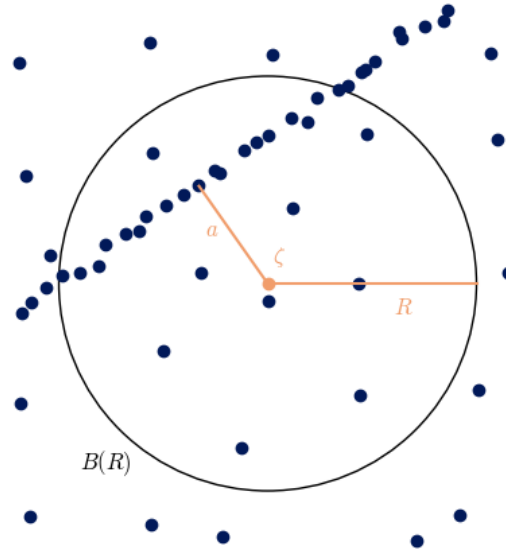
**Figure 6.** Picture of a situation where almost all points on the attractor (in dark blue) lie on a line. If the density of points is constant and denoted $\lambda$, the number of points inside $B(R)$ is essentially $2\lambda\sqrt{R^2 - a^2}$. For $a \ll R$, the estimated dimension will be 1.

for the Lorenz 63 system with $\rho = 166.5$, which is intermittent (Pomeau and Manneville, 1980; Sparrow, 1982). In the case of intermittent systems, a situation like the one displayed in Fig. 6 is often encountered, and the tools described in Section 2 can
360     be used to detect structures in phase space.

### 3.1    How we choose the values of $R$

It is difficult to chose relevant values of $R$ for each computation point $\zeta$ if we do not know the system. Indeed, depending on the dimension and on the density of points, the values of $R$ needed for $B(R)$ to contain a sufficient number of points to estimate $\delta$, might be different for each computation point $\zeta$.

365     An alternative approach is to compute the distance between the computation points and all other points of the trajectory and keep a given percentage $q$ of points, common to all computation points. For each computation point $\zeta$, $R$ is then defined such that $B(R)$ contains $q\%$ (i.e. the $q^{th}$ percentile) of the total number of points in the dataset. For each computation point and for each percentage $q$ for which we compute the dimension, there is thus one value of $R$. This has the advantage to adapt the range over which the dimension is computed accordingly to the computation point.

370     Of course, the percentile will not be exactly the same if one increases the length of the series. However, if the attractor has been reasonably sampled by $N_{tot}$ points, additional points should spread in the phase space in the same proportions, so that the percentiles computed with $N_{tot}$ or $N'_{tot}$ should correspond. In other words, if the density of points is already close to the

invariant measure of the attractor $\mu$, the computed percentiles will not significantly change when the length of the trajectory is increased.

375      In the following sections, we will use this method with percentages chosen evenly spaced on a logarithmic scale, typically with the maximum percentage being $10\%$ and the smallest percentage corresponding to 5 analogues. The dimension computed with 5 points will not give a precise value (see section 2.1.3) but this allows to ensure to have a dimension computed over a sufficiently large range of values of $R$. The values of the dimension with not enough points will be filtered out through the computation of $s$ and of the NRMSE score.

380      In section 3.3, we will also choose the values of the radius $R$, because it will be easier to illustrate the interpretation of the dimension in this case.

## 3.2    Lorenz 63 with $\rho = 28$

We start with the usual Lorenz 63 system with $\rho = 28$ (see Appendix A) and we consider two different trajectories: one with $N_{tot} = 10^4$ points, and the other one with $N_{tot} = 10^7$ points. Figure 7 shows the dimension computed with $q = 10\%$ (top, A

385 and B) $q = 1\%$ (bottom, C and D), for these two trajectories. For $q = 10\%$, the two plots look the same and the dimensions agree between the two datasets. This is because $10\%$ of $10^4$ is already enough points to estimate the dimension, and adding more points to the dataset will not change the percentiles, nor change the distribution of points on the attractor. Note that the points "on the border" of the attractor have higher dimensions since, from their point of view, the density of points is increasing. The estimated dimension for these points is actually an effective dimension reflecting this feature (see section 2.5).

390      On the other hand, for $q = 1\%$, there are not enough points in the $N_{tot} = 10^4$ dataset (Fig. 7 C) to have a proper estimation of the dimension, while the $N_{tot} = 10^7$ dataset (Fig. 7 D) still allows a proper estimation of the dimension. The latter gives more homogeneous values of the dimension than in the corresponding plot (7 B) with $10\%$ of the points. This is because the values of the percentiles are smaller, so that the estimation is more local and the density less varying in the balls $B(R)$.

     It is also interesting to analyze the histograms of the dimension for the $10^7$ points dataset, for $q = 1\%$ and $q = 10\%$ (Fig.

395 8): a lot of points have a dimension close to $1.5$ for $q = 10\%$, but most points have a dimension close to $2$ for $q = 1\%$. This is because, in the $q = 10\%$ case, $R$ is too large for some points: $2R$ is larger than the width of the wings of the attractor, so that the $C(R) \sim R^2$ cannot hold. Figure 8 illustrates this. In the $q = 1\%$ case, $R$ is smaller and this never happens.

     It is likely that, when decreasing $q$ and increasing $N_{tot}$ again in order to keep $N = qN_{tot}$ big enough, the dimension for all points will tend to a common value. This seems to be in agreement with the mentioned asymptotic results that the dimension

400 of almost all points converge towards a unique value.

     Indeed, as observed on Fig. 7, the dimension of the points on the wings seem to converge to some value close to $2$, as expected for a surface. As $q$ decreases and $N_{tot}$ increases, the dimension of the points on the "border" of the attractor will behave as others points on the wings and their dimension would converge to the same value close to $2$.

     The points close to the intersection of the wings have a dimension bigger than $2$ as long as their $B(R)$ includes this intersec-

405 tion. However, when is $q$ is decreased, the ball $B(R)$ might not anymore enclose the intersection. The neighborhoods of those
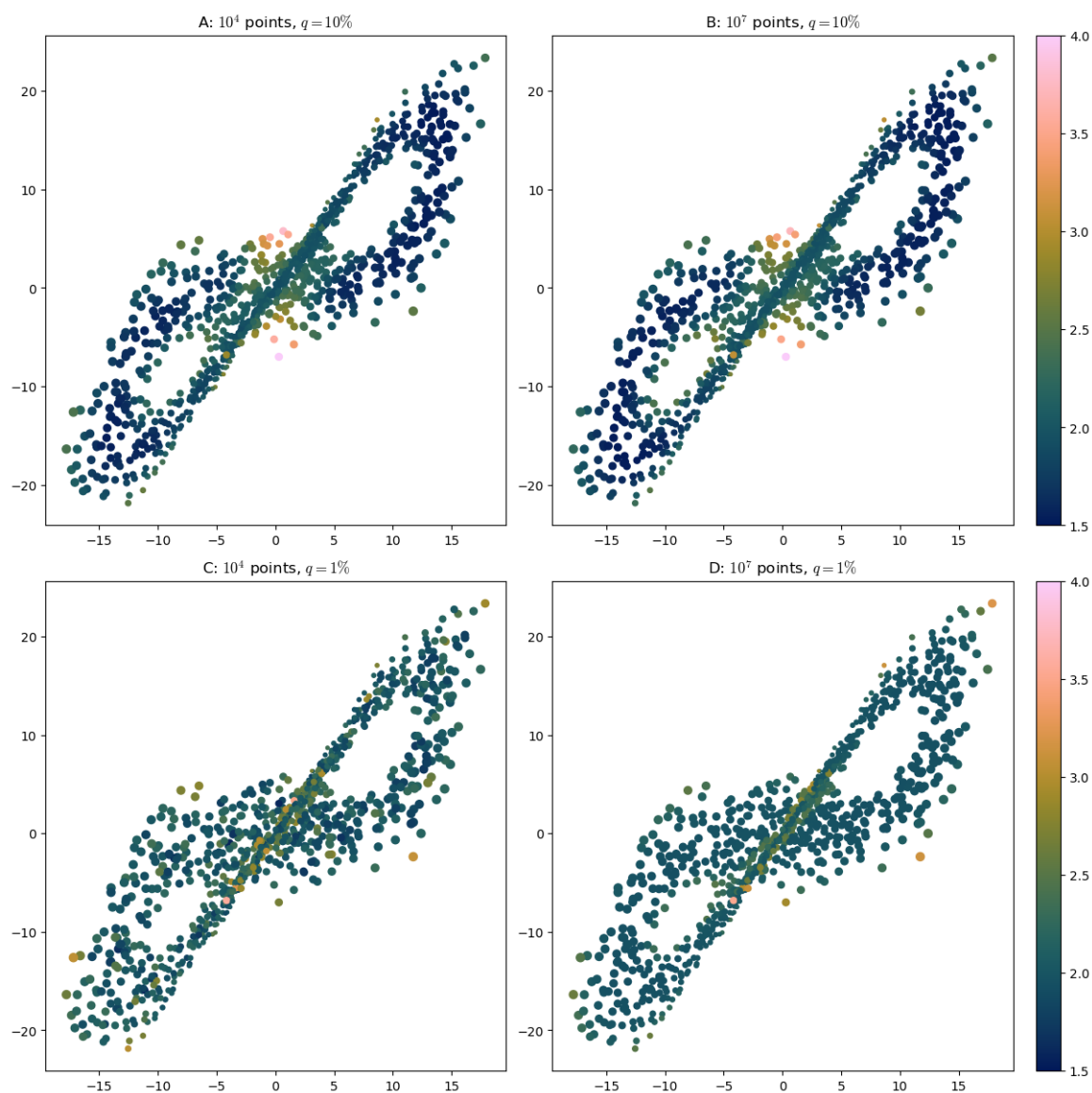
**Figure 7.** The Lorenz 63 attractor, with the dimension represented in color, computed with $10\%$ (top) and $1\%$ (bottom) of the points in each case (only the 1000 points for which the dimension has computed are represented).
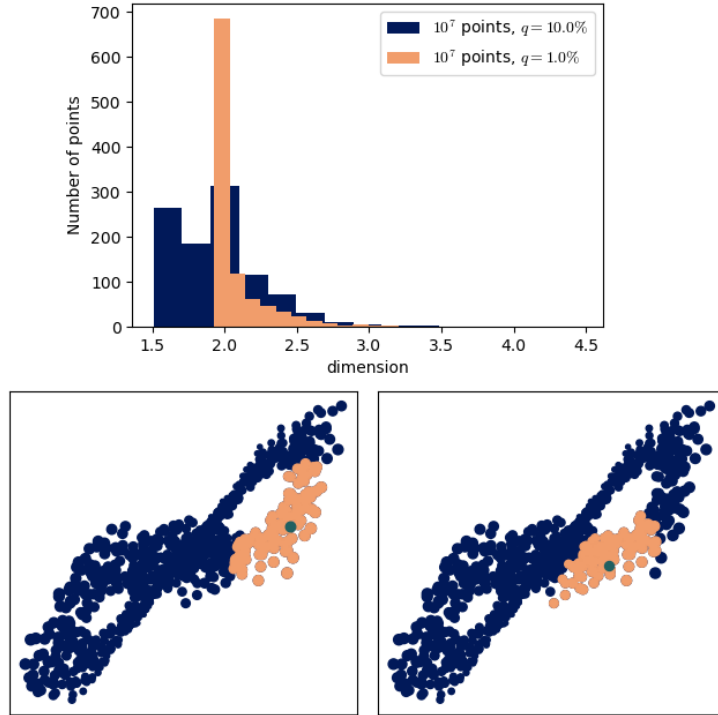
**Figure 8.** Top: Histograms of the dimension for the $10^7$ points dataset, for $q = 1\%$ and $q = 10\%$ (1000 values in each case). Bottom: Two illustrations that $R$ can be too large for $q = 10\%$. The computation point $\zeta$ is in green and some of the points used to compute the dimension are in orange. The ball $B(R)$ is bigger than the width of the wings, so that the $C(R) \sim R^2$ characteristic of a surface cannot hold.

points then look as that of any other points on the wings, so that their dimensions will be close to 2. Only the points exactly at the instersection will always have a $B(R)$ including this intersection, so that their dimension will never approach 2.

The left plot of Fig. 9 displays the dimension estimate $\hat{\delta}$ as a function of $R$. There is a range of values for which the $\hat{\delta}$ is close to 2 for all points. The curves having a bump in the middle of the range of values of $R$ correspond to points near the 410  intersection of the wings.

As one can see in the right panel of Fig. 9, some points with a high value of $s$ and a high number of points used in the estimation of $\delta$, have a poor NRMSE score (i.e. up to $0.4$, while most of the fits with $s > 10$ have their NRMSE score below $0.2$). Those correspond to situations shown in the bottom plots of Fig. 8, where the fit is not so good anymore, because the scaling is $\sim R^2$ for small $R$ but not for higher values of $R$.

415  ### 3.3  Lorenz 63 with $\rho = 166.5$

The local dimension applied to the intermittent Lorenz 63 system with $\rho = 166.5$ is now analyzed (see Appendix A for a short presentation). The case of intermittent systems is interesting since those systems have a strongly inhomogeneous phase space,
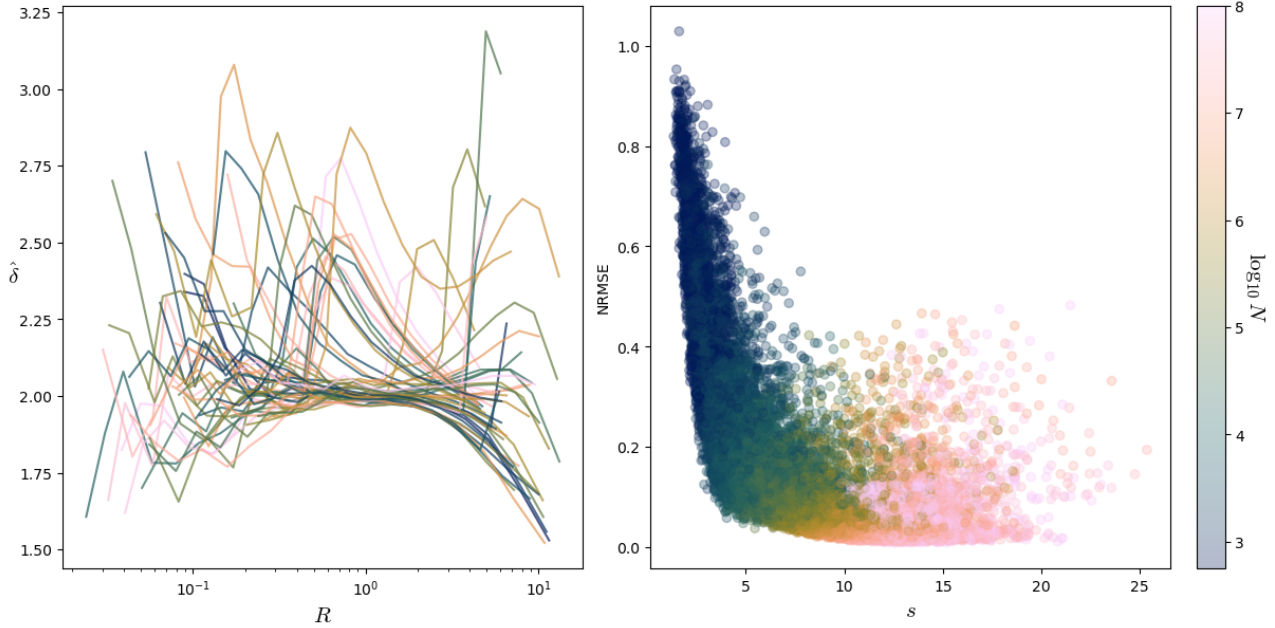
**Figure 9.** Left: Plot of $\hat{d}$ versus $R$ for 50 points of the Lorenz 63 system ($\rho = 28$) with $10^7$ points (NRMSE$< 0.4$, $s > 5$). Right: scatter plot of NRMSE vs $s$ for the same dataset, but for all 1000 computation points. The color represents the logarithm of the number of points used in the dimension estimation.

allowing to illustrate how the dimension can have different values at different scales $R$. Intermittent systems are also of special interest, since the primary goal is to use the local dimension on the rain data, which is known to be intermittent.

420      This system was integrated for $\rho = 166.5$ to obtain $10^6$ points on the attractor and the dimension was computed for 1000 points. The plot of the dimension against $R$ (computed as percentiles) is in the left panel of Fig. 10. One can see that, for the smallest values of $R$, the dimension is around 2, while it is closer to 2 for the highest values of $R$.

     Actually, the remaining of the attractor before the bifurcation (see Fig. A1) defines a $1-$dimensional structure in phase space, so that we expect that in the balls $B(R)$ intersecting enough this closed loop, the scaling will be strongly influenced by

425 this closed loop (as described in Section 2.5). A better insight of the behavior of the dimension with $R$ than that given by Fig. 10, can be gained by characterizing each point by its position with respect to this closed loop.

     To do so, we select a part of the trajectory where it seems regular and almost periodic, and integrate this part of the trajectory with a very small timestep. We then take this as a representation of the laminar regime. Of course, the trajectory is not strictly periodic, so choosing different parts of the trajectory will lead to slightly different representations. This representation allows

430 to define the "laminar distance" for any point $\zeta$ in the trajectory, as the smallest of the distances between $\zeta$ and all points in the representation of the laminar regime. From a dynamical point of view, points with small laminar distances will be considered as points in the laminar regime, while points with a significantly non-zero laminar distance can be considered as chaotic points.
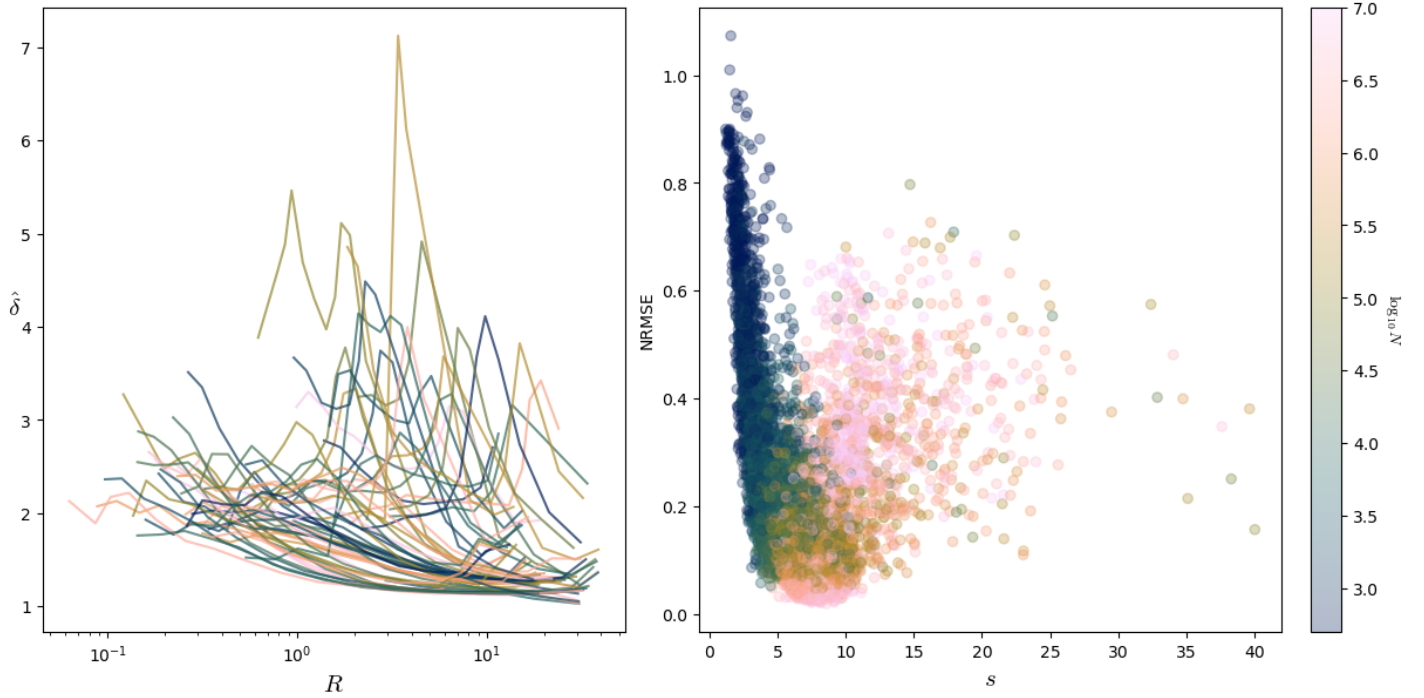
**Figure 10.** Left: estimated dimension $\hat{\delta}$ against $R$ for the intermittent Lorenz 63 ($\rho = 166.5$, $10^6$ points). Only fits with NRMSE$< 0.4$ and $s > 5$ are shown. Right: scatter plot of NRMSE vs $s$ (all fits).

Figure 11 shows the dimension as a function of the laminar distance for that point. More specifically, 6 values of the radius $R$ ($R = 2, 5, 10, 15, 20, 30$) were whosen and the dimension for 1000 computation points is computed. Each panel corresponds to a specific radius $R$. In addition, the red vertical line marks where the laminar distance is equal to the radius $R$ used in this plot.

One can see from Fig. 11 that the dimension peaks for points whose laminar distance equals $R$. In other words, from the point of view of a given point:

– when $R$ is smaller than the laminar distance, the dimension is around 2,

– when $R$ equals the laminar distance, the dimension has a peak,

– when $R$ is bigger than the laminar distance, the dimension decreases between 1 and 2.

The fact that there is a peak in the dimension when $R$ equals the laminar distance can be understood by noting that it corresponds to the entrance of the laminar structure in the $B(R)$ ball around the computation point $\zeta$. There are suddenly a lot of points in the ball, near the boundary of the ball, so that the distribution of points in $B(R)$ resembles more the dark blue curve than to the orange curve in Fig. 3.

**21**
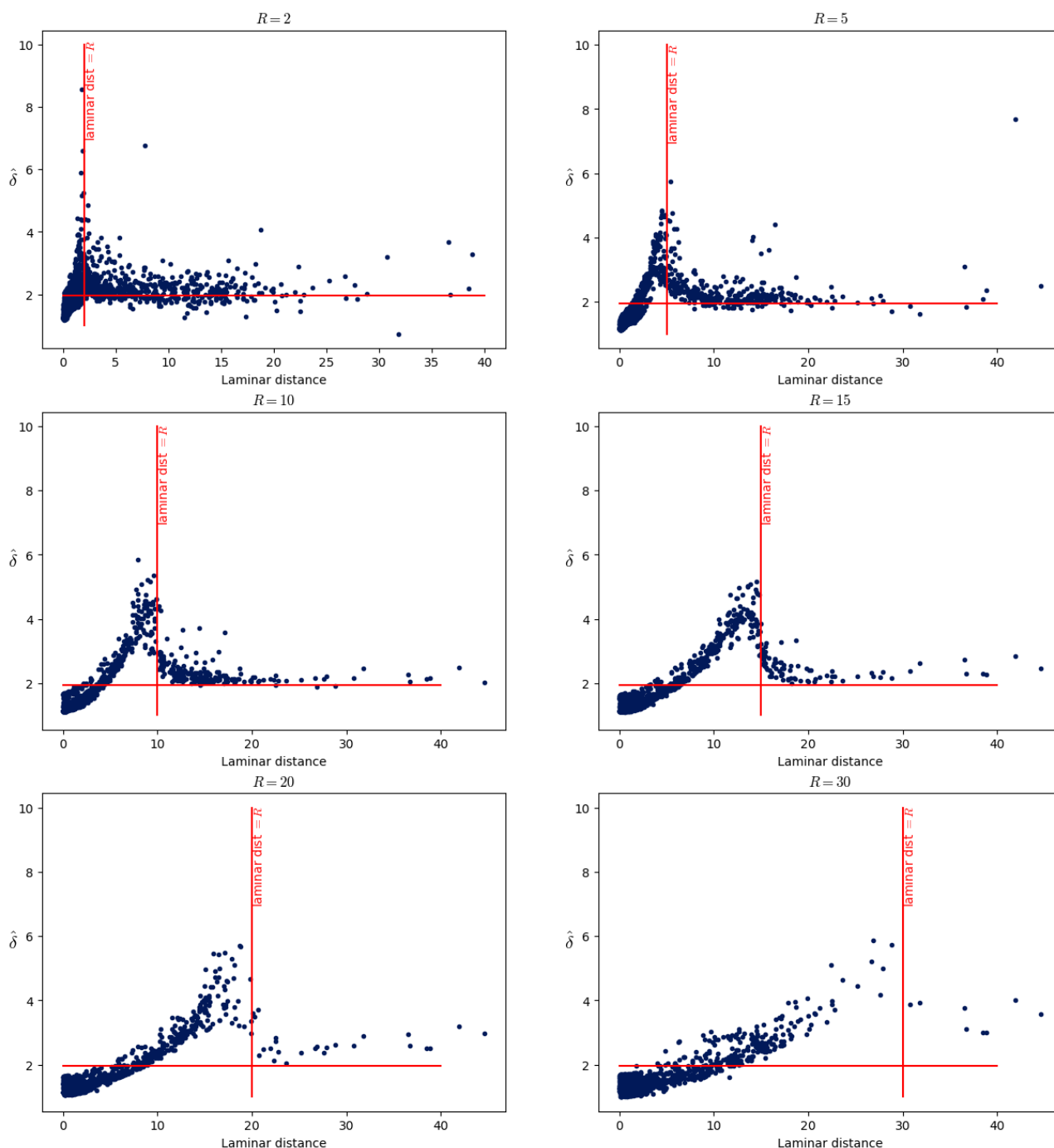
**Figure 11.** Scatter plots of the local dimension in terms of the laminar distance. In a plot, all the dimensions have been computed with the same radius $R$ (the value is above the plot). The red horizontal line marks the dimension value equal to 2, while the vertical red lines marks the value of the laminar distance which is equal to the radius $R$.
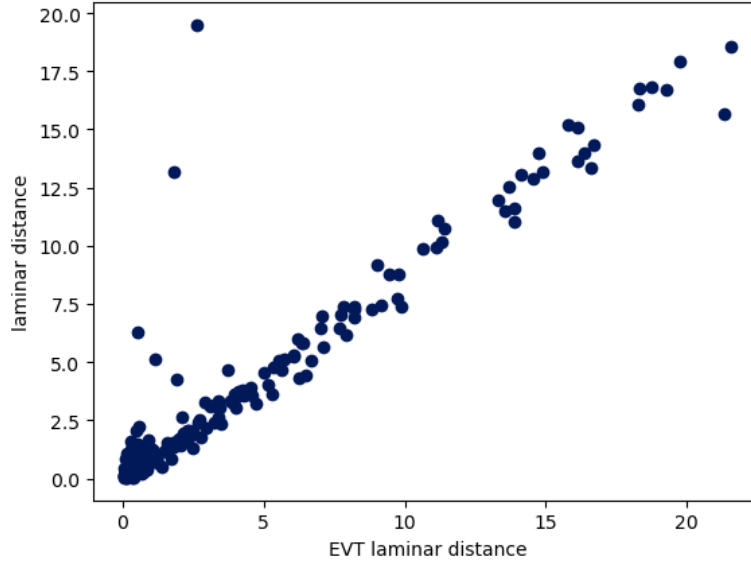
**Figure 12.** Comparison of the EVT laminar distance with the laminar distance for the intermittent Lorenz 63 ($\rho = 166.5$). The EVT laminar distance is computed as the distance for which the dimension is maximum (see text).

When $R$ is bigger than the laminar distance, the situation becomes similar to the one in Fig. 6 and the dimension becomes closer to 1. The dimension is 1 only if $R$ is sufficiently bigger than the laminar distance (equivalently, $R \gg a$ in Fig. 6), which can happen only for points sufficiently close to the laminar regime. For other points, other parts of the loop forming the attractor in Fig. A1 would enter the $B(R)$ ball and modify the scaling, or the curvature effects become to important. In those cases (when 450 $R$ is bigger than the laminar distance, but not much bigger), the distribution of points in $B(R)$ is not close to a power law, so that the exponential fit is not appropriate.

When computing the dimension in the asymptotic limit, the radius $R$ should be below any other geometric scale around the computation point $\zeta$. For the chaotic points, this geometric scale is their laminar distance, while for laminar points, the geometric scale would be the "width" of the laminar structure in phase space.

455 As a concistency check for that interpretation, we tried to estimate the laminar distance for each of the 1000 computation points as the value of the radius $R$ for which the dimension is maximum. For these 1000 computation points, we computed the radii $R$ as percentiles, the corresponding dimensions, and their laminar distance. In order to use only meaningful values of the dimension, for each computation point, we restricted the dimension to the range of values of $R$ where NRMSE$< 0.5$ and $s > 4$. We rejected all estimations where the maximum was found on one of the end of this range because this points to the fact 460 the true peak of the dimension is maybe not in this range of values. Because of that, the laminar distance could be estimated for only one fourth of the 1000 computation points. The scatter plot in Fig. 12 shows the comparison of the laminar distance to this estimation of the laminar distance using EVT ("EVT laminar distance").

23

Note that the EVT laminar distance tends to be bigger than the laminar distance. This is because, if $R$ is precisely equal to the laminar distance, there are not enough points in $B(R)$ for $\hat{\delta}$ to be really influenced. $R$ has to be a little bigger than the laminar distance for $\hat{\delta}$ to really increase, and the dimension of $\hat{\delta}$ is for values of $R$ a little bigger than the laminar distance.

We carried out the same analysis on two other intermittent dynamical systems: the Lorenz 96 system with $n = 4$ variables for $F = 11.87$, and the Lorenz 96 system for $n = 12$ variables for $F = 4.4$. Figures similar to 11 for those two systems are displayed in Appendix B.

## 4 Application to large systems

In this section, we present the results of the computation of the dimension for two large systems: the Lorenz 96 system with $n = 50$ dimensions and the RADCLIM dataset (radar images of the precipitation field).

### 4.1 Lorenz 96, $n = 50$

The Lorenz 96 system (see Appendix B for a brief description) with $n = 50$ and $F = 4.9$ was integrated for $t_{max} = 10^6$, with a timestep of $dt = 0.1$. This gives a total number of points of $N_{tot} = 10^7$ points in the trajectory. The radii $R$ are computed as percentiles and the corresponding estimates of the dimension are computed.

The right plot of Fig. 13 shows as expected that the NRMSE score decreases when $s$ is increased. The left panel of Fig. 13 shows the estimated local dimension against the radius $R$ of the ball for 100 points in this system. The more a curve starts at a high value of $R$, the more the corresponding points is alone in phase space. We selected the points for which the NRMSE is smaller than $0.4$ and $s > 6$. One can see at the bottom of the plot a set of curves having all a small maximum for radii between 8 and 12, and maximum dimension smaller than $\sim 12$ (dotted curves).

These points seem to detect a structure of points at a distance $10 - 12$ from them. If there was such a structure at that distance, we would see other curves with maxima for small values of $R$ for the points which are part of this structure, as for the intermittent Lorenz 63 in section 3.3. Since there are no such curve, because the dotted curves look quite regular, and also because they correspond to a great proportion of all the curves, we can think that the points corresponding to these curves are part of the detected structure. In other words, the dotted curves correspond to points which are part of the structure that these curves detect. Geometrically, the points of these curves have a similar role than the laminar points of the section 3.3.

To understand how a structure can be detected by the curves of the points which are part of that structure, consider points uniformly distributed on a circle of radius $\tilde{R}$. From the point of view of a point on the circle, the number of points at a distance $< R$ grows as $\tilde{R} \arccos\left(1 - \frac{R^2}{2\tilde{R}^2}\right)$. This curve is the steepest when $R$ approaches $2\tilde{R}$, so that the fitted $\delta$ would have a peak for $R \sim 2\tilde{R}$. This peak is analogous to the peak of the dotted curves in the left plot of Fig. 13.

The curves which are not in this set are much more diverse. They all start at a higher value of the radius, which is because the corresponding points are in less dense parts of the phase space. Typically, their starting value of $\hat{\delta}$ is also higher, and this is because the density of points around those points typically increases. This leads to artificially high values of $\delta$ (see $\delta_{eff}$ of section 2.5). Some of these curves have a bump: these could be because the previous structure enters their ball, and the radius
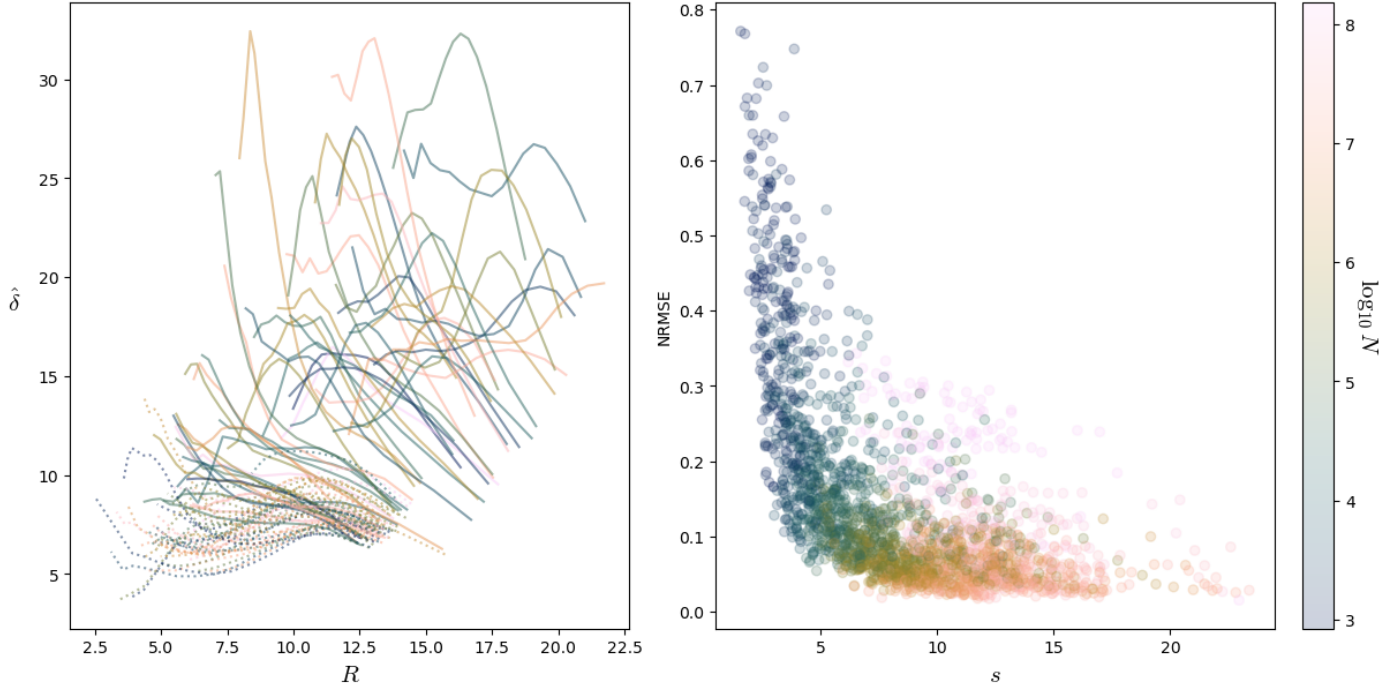
**Figure 13.** Left: Scatter plot of the NRMSE vs $s$ for the Lorenz 96 system with $n = 50$ and $F = 4.9$, with $\log_{10} N$ in color. Right: Plot of the dimension against the radius $R$ for 100 computation points for Lorenz 96 with $n = 50$ and $F = 4.9$. Each curve is, for one point, the computed dimension against the radius of the ball. We selected the points for which the NRMSE is smaller than $0.4$ and $s > 6$. The dotted lines detect a structure and the corresponding points are part of that structure.

for which this happens would then be the distance of the corresponding points to the structure (laminar distance of the section 3.3).

To further clarify this viewpoint, a trajectory of this system with $10^5$ points was generated and the dimension is computed for all points. The $10^5$ points were labelled as laminar or chaotic, with the following steps:

1. restrict the curve for radii $R > 8$;

2. look for the maximum of this restricted curve;

3. if this maximum is not at the ends of this curve, and if the value of the dimension at the maximum is smaller than $12$, the point is labelled as laminar.

Points not labelled as laminar are labelled as chaotic. Note that the laminar/chaotic points are not necessarily laminar/chaotic in the context of chaotic intermittency in dynamical systems, but we use this terminology to distinguish points with different dimension characteristics.
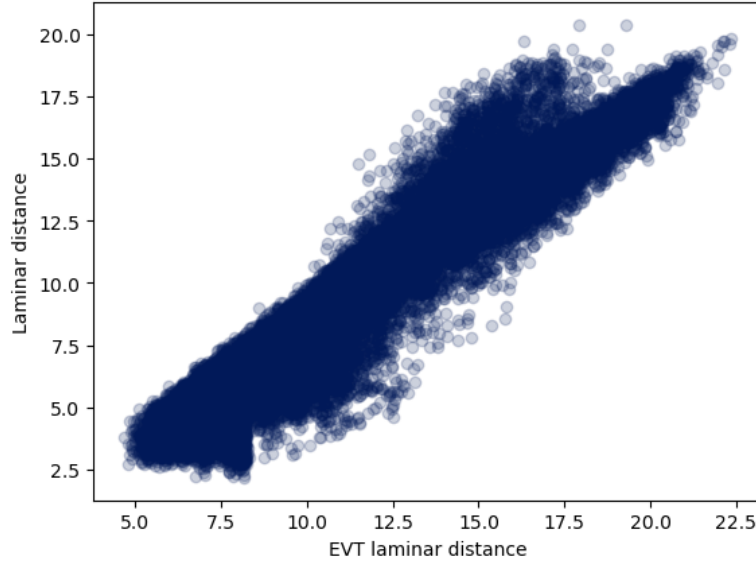
**Figure 14.** Scatter plots of the two ways to compute the distance to the laminar structure.

If the points we have labelled as laminar indeed form a geometric structure in phase space, the distance of chaotic points to this structure should correspond to a maximum of the dimension. Therefore, we proceed as in section 3.3: for each chaotic point,

1. we define the laminar distance as the minimum distance between the point and all the laminar points (in other words, using the points labelled as laminar as a representation of a laminar regime).

2. we define the EVT laminar distance as the radius $R$ giving the maximum dimension.

If our above labelling of laminar and chaotic points is meaningful, the two distances should agree. As shown in the scatter plot of Fig. 14, there is a good agreement and we take this as a consistency check of our interpretation of the curves in the left panel of Fig. 13.

Note that, for $32.8\%$ of the chaotic points, no distance could be computed using the second way (for the same reason than in section 3.3). Also, the fact that we find a structure in phase space, analog to the laminar structures of the previous sections, points to the fact that the Lorenz 96 system for this value of $F$ could be in an intermittent regime.

To summarize, we computed the dimension in this high-dimensional system. As shown in the previous section 3.3, the dimension highly depends on the radius $R$ used to compute it, but this can be used to obtain some characterization of the geometry of the phase space: some points of the attractor are collected in a structure, much as the laminar points in section 3.3. The distance from the other points to this structure can be estimated.
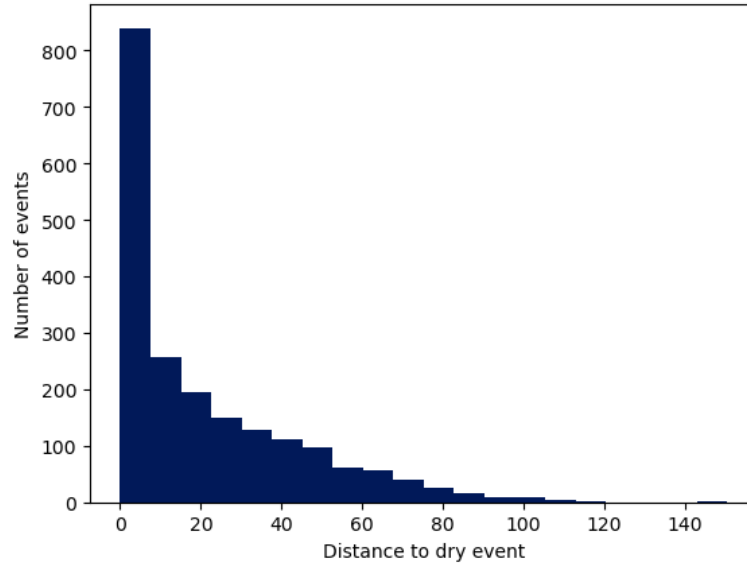
**Figure 15.** Histogram of the distances to the dry event for the RADCLIM dataset.
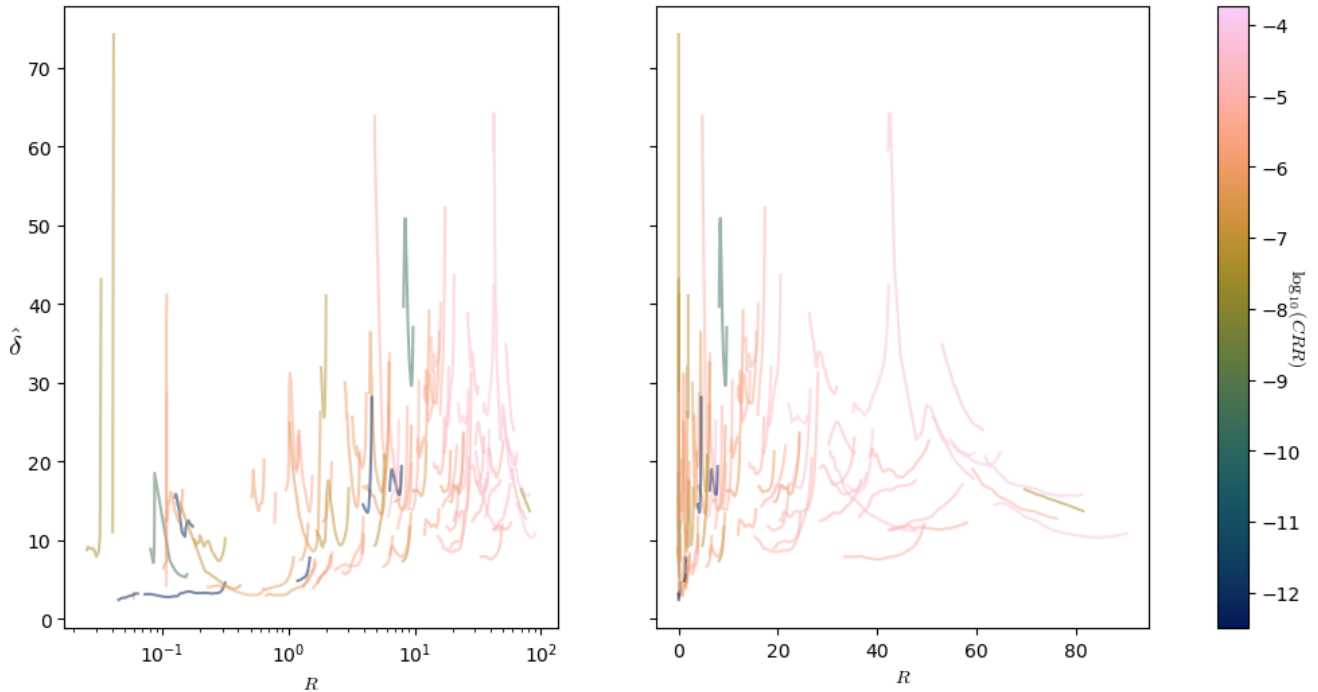
## 4.2 RADCLIM dataset

We now present the results of the computation of the dimension for the RADCLIM dataset (see Appendix C for a description). Before computing the dimension, the images were upscaled to 14x14 for two reasons. The first is that the whole dataset is then obviously easier to work with. The second is based on the hope that the upscaled images would define a reduced and less complex attractor, with smaller values of the local dimension.

The upscaling to 14x14 images was done by averaging the neighbouring pixels, after the log-transform of the rain rate. This is a way to take into account the multiplicative structure of the rain (Veneziano et al., 2006; Seed, 2003; Lovejoy and Schertzer, 2013) during the upscaling. As in Pulkkinen et al. (2019b), the zeros were transformed to -15 in logarithmic scale.

The geometry of the phase space defined by these images is quite particular. The value of each pixel is taken as an axis in phase space, which is therefore a 14x14 = 196 dimensional euclidean space. Since the minimum value for all pixels is -15, the phase space is actually restricted to the orthant defined by $x_i \geq -15 \ \forall i = 1, ..., 196$. There are 7150 ($= 1.13\%$ of 630008) images without any rain (i.e. dry event, $x_i = -15 \ \forall i$). Even among images with rain, most of them are close to the dry event. The histogram in Fig. 15 shows the distribution of all distances to the dry events (including the dry events themselves).

This histogram shows that the density of points in phase space decreases very quickly when getting away from the dry event. As a comparison, if the density of points $\rho$ was constant in phase space, the number of points whose distance to the dry event is between $r$ and $r + dr$ would be $\approx \rho r^{n-1} dr = \rho r^{195} dr$. This means that the heights of the sticks in this histogram would grow as $r^{195}$, which is radically different than what is observed! The relationship between distances and volumes in high-dimensional spaces can be quite different than our 3-dimensional intuition.

**Figure 16.** Plot of the dimension against the radius for 100 points for the RADCLIM data (NRMSE$< 0.4$ and $s > 5$)

540      For 2000 computation points, the dimension was computed for 40 different values. As before, 40 percentages were fixed (exponentially spaced between $8 \times 10^{-4}\% \rightarrow 5$ points and $10\% \rightarrow 63\,000$ points), and the radii were chosen to correspond to the percentiles among all distances. Figure 16 shows the computed dimension as a function of the radius $R$ for 100 points: the left plot has a logarithmic scale for $R$ and the right plot has a linear scale for $R$, allowing to see more clearly the plot for small $R$ values or for large $R$ values. The color represents the 10-logarithm of the averaged convective rain rate (see below).

545      For some of the 2000 points, there is a bump in the dimension, which would point to the existence of some structure. We tried to apply the same procedure as in section 3.3 to compute the distance to the laminar regime. The procedure outputted a laminar distance for only 487 out of 2000 points (for the same reason than in section 3.3: we discarded the estimation if the maximum dimension is on one of the ends of the range). It turns out that the laminar distance is highly correlated to the distance to the dry event: see Fig. 17. As a consequence, the points labelled as laminar would simply be the dry events, or events which

550 are almost dry. The laminar distance as defined in this way does not really seem to contain any additional valuable information than the distance to dry events.

     In order to check if there is any valuable information in the set of values of $R$ for one computation point, we computed the mean and the median of $R$ for all points. Note that these quantities obviously depend on the way the percentages to compute the dimension for were chosen. Because of that, one could think that this mean and this median would not be very informative.

555 These values are however relatively stable: we checked for example that they do not change much if we use the 10 smallest
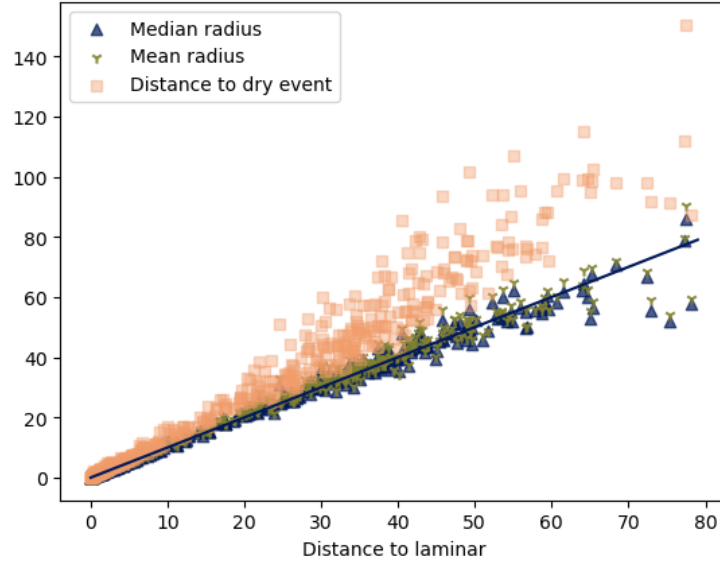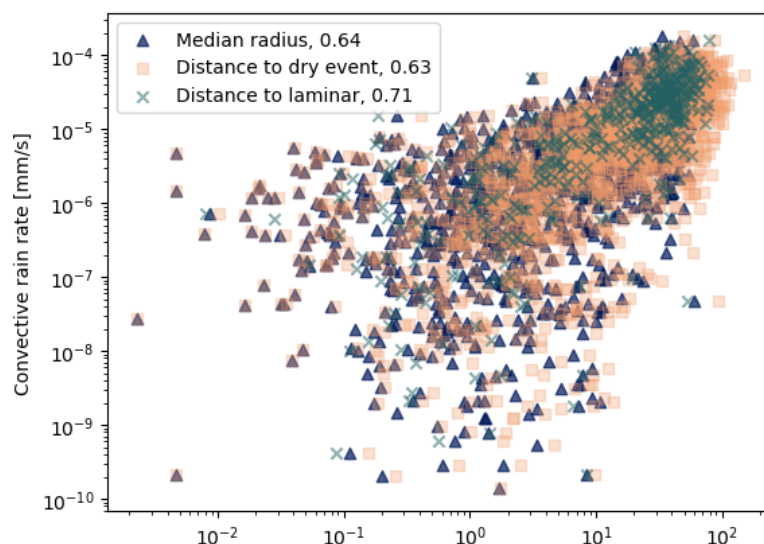
**Figure 17.** RADCLIM data: the laminar distance on $x-$axis, with the median radius, the mean radius and the distance to the dry event on the $y-$axis.

radii for each point, instead of the 40 we have. This is because the extent of the range of values of radii is small with respect to the actual values of the radii. This also is why the mean and the median does not differ much, and why they give a measure of the relevant values of the radius for each point. Figure 17 shows that there is a correlation of these two quantities with the laminar distance and the dry distance. This shows that these 4 quantities (median radius, mean radius, laminar distance, dry distance) are essentially the same.

We see here the difficulty to work with high-dimensional systems, as discussed in the section 2.4. The particular geometry of this phase space worsens even more the situation, because most of the points are collected near the dry event, as shown in the histogram of Fig. 15. Because of this, the dimension for all points can only be computed reliably on quite small range relatively to the values of $R$ involved. For example, the points for which the curves are on the left of Fig. 16 have often $R$ approximatively within $[30, 40]$. This is a too small range of values of $R$ to properly interpret the computed values of $\delta$. The same happens for the points for which the curves are on the right of the figure: they have often $R \in [80, 100]$.

We used the convective available potential energy (CAPE), the convective rain rate (CRR) and the convective precipitation (CP) data from the ERA5 reanalysis to compare with the quantities computed in the phase space. For the region covered by the RADCLIM dataset, they come in 26x41 images with a 1-hour resolution. We computed the mean of these images in order to have one value for each hour. For each of the 2000 computation images, we associated the closest in time available value of the CAPE, the CP and the CRR. As suggested by the color grading in Fig. 16, one can find a correlation between the mean radius, the dry distance or the laminar distance on one hand, and the CRR on the other hand: Fig. 18 shows the corresponding scatter plots for the 2000 images.

**Figure 18.** RADCLIM data: scatter plots of the mean radius, the dry distance and the laminar distance ($y-$axis) with respect to mean convective rain rate (CRR) ($x-$axis). The numbers in the legend are the correlation coefficients of the 10-logarithm of each of these distances with $\log_{10}(CRR)$.

Results with the CP instead of the CRR are very similar, while the correlations with the CAPE also exist but are not as good.

575    The correlation of the CRR is the highest with the laminar distance but this is because of the restriction to some points. The laminar distance could indeed be computed for only 487 points out of 2000, while the mean radius and the dry distance can be computed for all the points. If we restrict the computation of the correlation between the CRR and the mean radius to the points for which a laminar distance was computed, one gets a correlation of $0.70$. The same happens for the correlation between the CRR and the dry distance.

580    We checked also if some information can be extracted from the mean value of the dimension: for each image, we computed the mean of the dimensions whose NRMSE score was below $0.4$ and $s$ above $5$. Figure 19 shows the histogram of the repartition of this mean dimension for our 2000 computation images (in orange) and the scatter plot of this mean dimension with the CRR (in color grading from dark blue to orange). A complementary 2D histogram of the mean dimension with to the CRR is shown in Appendix C (Fig. C1).

585    A few things can be noted here:

  – the histogram has a nice peak around a mean dimension of 15-20;

  – the relationship with the CRR is not very clear, except that there is generally less variability in the CRR when the dimension is higher;

  – as expected, images the farther away from the dry event have the higher CRR, but those images do not have the highest
590       values of the mean dimension: their mean dimension is rather between 10 and 20;

**30**
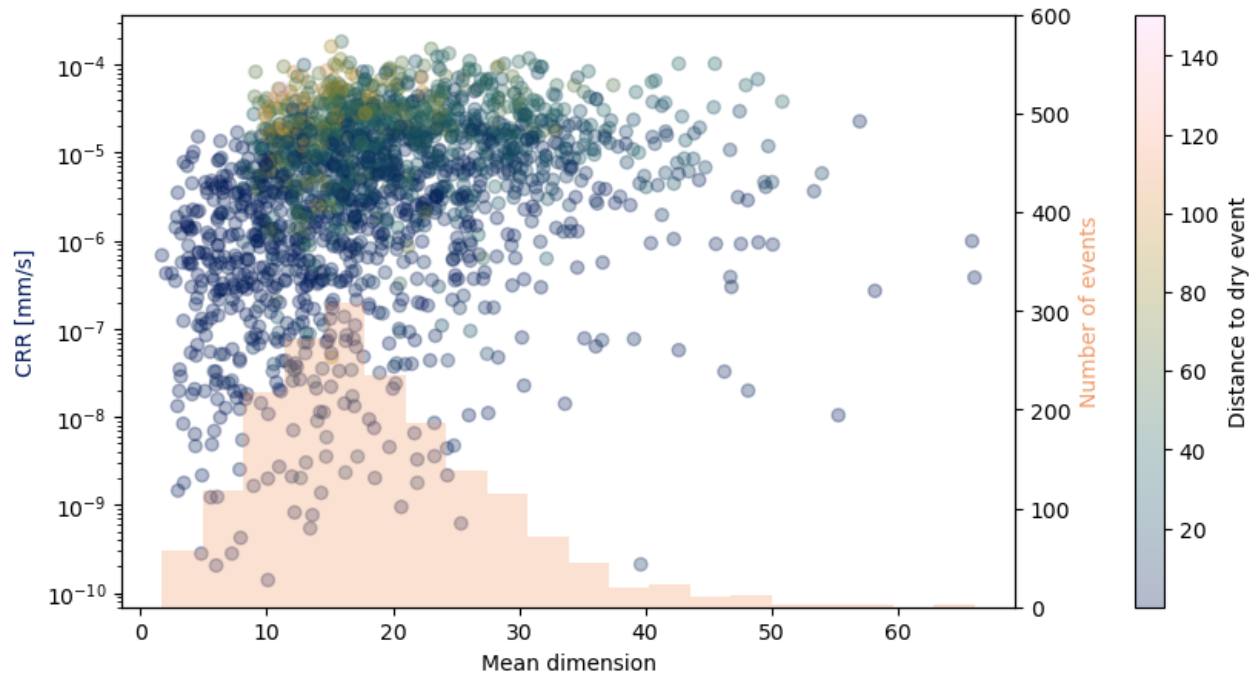
**Figure 19.** Histogram of the repartition of the mean dimension for our 2000 computation images (in orange) and scatter plot of this mean dimension with the CRR (in color scale). The color is the distance to the dry event.

- when the mean dimension is below 10, the distance to the dry event is always relatively small (i.e. for big enough distances, the dimension is always above 10); this can also be seen from Fig. 16 taking into account that the distance to the dry event is almost the same than $R$.

This analysis of the results of the computed dimension for the RADCLIM dataset shows that it is possible to compute reliably the dimension for some points and for some radii $R$, but the results are quite difficult to interpret, essentially because of the limited number of data with respect to the number of dimensions at play. The estimated local dimensions ranges between 10 and 30, with a peak around 15-20. Not surprisingly, we observed a link between the convective rain rate and the distance to the dry event.

## 5 Summary and discussion

As emphasized in the introduction, results on the local dimension of attractors of dynamical systems predict that all points have the same dimension in the asymptotic limit. The local dimension for finite $R$ allows to detect geometrical structures in phase space of chaotic dynamical systems.

When working with such tools, one always faces the question to know if the estimation of the dimension is reliable or not. This question is linked to that of the maximal dimension that one can estimate with a given number of points inside $B(R)$. We

605  systematically used the NRMSE score and the quantity $s$ to tackle this problem. The development leading to the definition of $s$ brought some light on the problem of the maximal measurable dimension using EVT techniques. This gives some falsifiability methods, which were lacking before, as was noticed in Datseris et al. (2023).

In short, the dimension is estimated as the exponent of the power law $C(r) \sim r^\delta$ over a some range $[0, R]$. If the NRMSE score is good enough, a $10\%$ accuracy for $\delta$ is achieved with $N \gtrsim 400$ points. However, a high exponent in the scaling $C(r) \sim$

610  $r^\delta$ (i.e. a high dimension) will not be visible over a long interval $[0, R]$ if there is not enough points. This is why high dimensions may be estimated, but only on limited ranges. There is no contradiction with the argument of (Eckmann and Ruelle, 1992) : for a fixed range $[0, R]$, the number of points needed to measure a dimension indeed grow exponentially with the dimension. The same applies for the correlation dimension: for a fixed number of points, higher dimensions can be measured if the range $[0, R]$ decreases.

615  As shown, the dimension depends on the finite radius $R$ of the ball $B(R)$ used to compute the dimension. This implies that one cannot simply choose some small percentage (as $2\%$ or $5\%$), compute $R$ as the corresponding percentile and get a unique value for the dimension. In fact, different finite values of $R$ may lead to very different values for the dimension.

To understand what is captured by the computed dimension at a given scale $R$, one has to compare $R$ with the other local geometrical scales on the attractor. In this work, these scales were mainly set by some geometrical structures, but Perinelli et al.

620  (2023) showed that the curvature could also set some scale, and the idea that the scale of the noise could play a role was raised by Little et al. (2017). We also identified that estimations of the dimension can be affected when the density of points is not constant. This often leads to an overestimation of the dimension. The value of the dimension for a given $R$ can be affected by yet other phenomena, and it is important to recognize which ones are at play to interpret correctly the dimension.

For the RADCLIM dataset, one difficulty is that the number of points is rather limited so that, for each computation point,

625  values of the dimension could only be computed in a very limited range of values of $R$. This was expected from the analysis of Section 2.4, and this makes difficult the interpretation of the value of the dimension for this high-dimensional system. Some interesting conclusions could however be gathered from the analysis, in particular that the range of dimension is between 10 and 30 with a peak at 15-20.
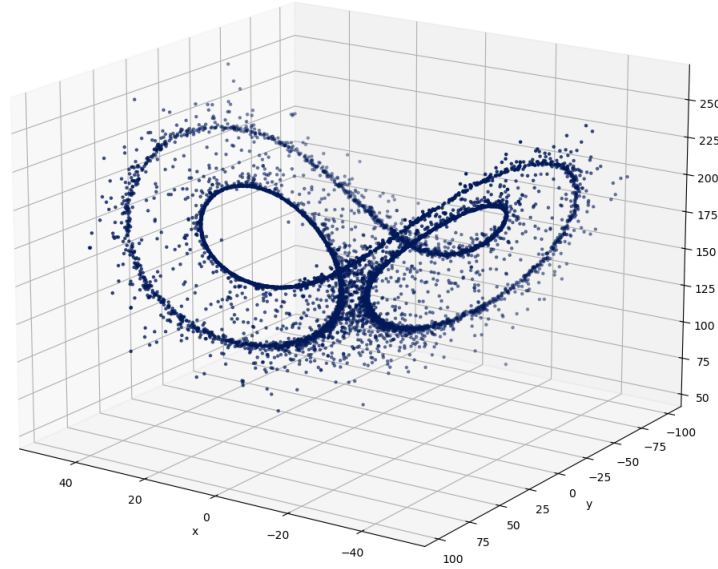
## Appendix A:  Lorenz 63 system

630  The Lorenz 63 system is defined by the following equations (Lorenz, 1963)

$$\begin{cases} \dot{x} &= \sigma(y - x) \\ \dot{y} &= \rho x - y - xz \\ \dot{z} &= xy - \beta z \end{cases} \tag{A1}$$

where $\sigma, \beta$ and $\rho$ are constant. Usual values are $\sigma = 10$, $\beta = 8/3$ and $\rho = 28$. In this configuration, the system is known to be chaotic.

**Figure A1.** Lorenz 63 attractor for $\rho = 166.5$. The remaining of the attractor before the bifurcation is visible.

The same system for $\rho = 166.5$ was also considered ($\sigma$ and $\beta$ being unchanged). This system is known to be intermittent,
635    meaning that it follows regular patterns for some periods of time (so-called "laminar" phases), alternating with other periods
where it seems to behave randomly (the "chaotic bursts"), see Ott (2002); Schuster and Just (2006); Elaskar and Rio (2017)
about intermittent dynamical systems. A trajectory is displayed in Fig. A1.

As was first noted in Pomeau and Manneville (1980), this system undergoes a bifurcation for $\rho \approx 166.07$: the attractor is
first periodic but disappears through a saddle-node bifurcation (Sparrow, 1982). The regular pattern followed during laminar
640    phases after the bifurcation is the remaining of the attractor before the bifurcation.

## Appendix B:  Lorenz 96 system

The Lorenz 96 system (Lorenz, 1996) is a dynamical system with $n$ variables $x_i$ for $i = 1, \ldots, n$ ($n \geq 4$). The evolution equations for the $x_i$'s are

$$\dot{x}_i = (x_{i+1} - x_{i-2})x_{i-1} - x_i + F \tag{B1}$$

645    where index $i$ is understood as periodic: $x_{-1} = x_{n-1}$, $x_0 = x_n$ and $x_{n+1} = x_1$. The parameter $F$ is a forcing constant.

This system for $n = 4$ goes through a saddle-node bifurcation at $F \approx 11.83$ (Sterk and van Kekem, 2017; van Kekem and
Sterk, 2018) and is intermittent after (see Appendix A for a brief introduction on intermittency). Figure B1 shows that the
estimated value of $\delta$ is maximum when the laminar distance is equal to $R$, as in Fig. 11.
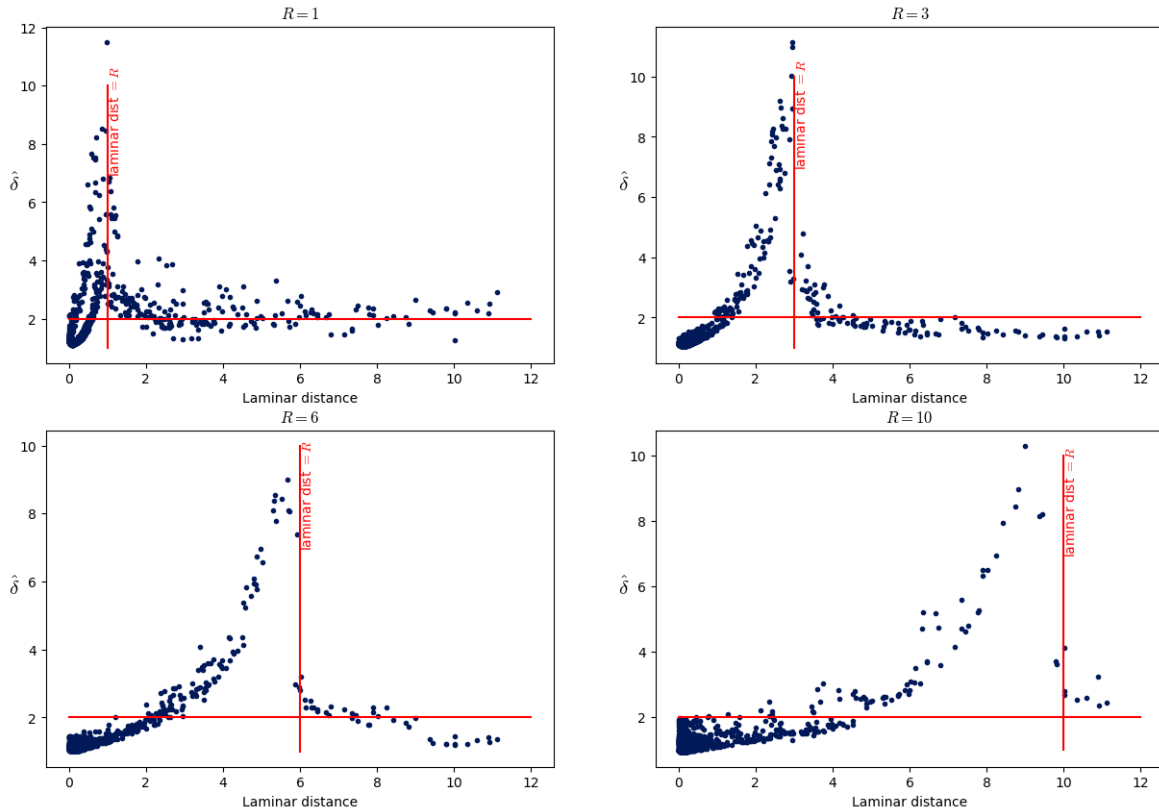
**Figure B1.** Same as Fig. 11 but for the Lorenz 96 system with $n = 4$ and $F = 11.87$ ($10^6$ points in the trajectory). The vertical red lines marks the value of the laminar distance which is equal to the radius $R$ and the horizontal line marks the values 2 for $\hat{\delta}$.

We also considered the Lorenz 96 system with $n = 12$. We found a bifurcation at $F \approx 4.25$ with an intermittent behavior after this value. The attractor before the bifurcation is multi-dimensional, and so is also the laminar regime in this case. Because of this, the trajectory in laminar phases is not almost periodic and one cannot proceed as we did for Lorenz 63 with $\rho = 166.5$, to get a representation of the laminar regime. Instead, we used a trajectory for $F = 4.2$ to represent the laminar regime. The problem with this appraoch is that the laminar regime after the bifurcation has moved and expanded in phase space with respect to the attractor at $F = 4.2$. The peak of the dimension when the laminar distance is equal to $R$ is still clearly visible in Fig. B2.

## Appendix C: RADCLIM dataset

The RADCLIM radar dataset (Goudenhoofdt and Delobbe, 2016; Journée et al., 2023) is a high horizontal and temporal resolution quantitative precipitation estimation in Belgium and its surroundings. It is based on radar measurements, which are merged with rain gauges measures.
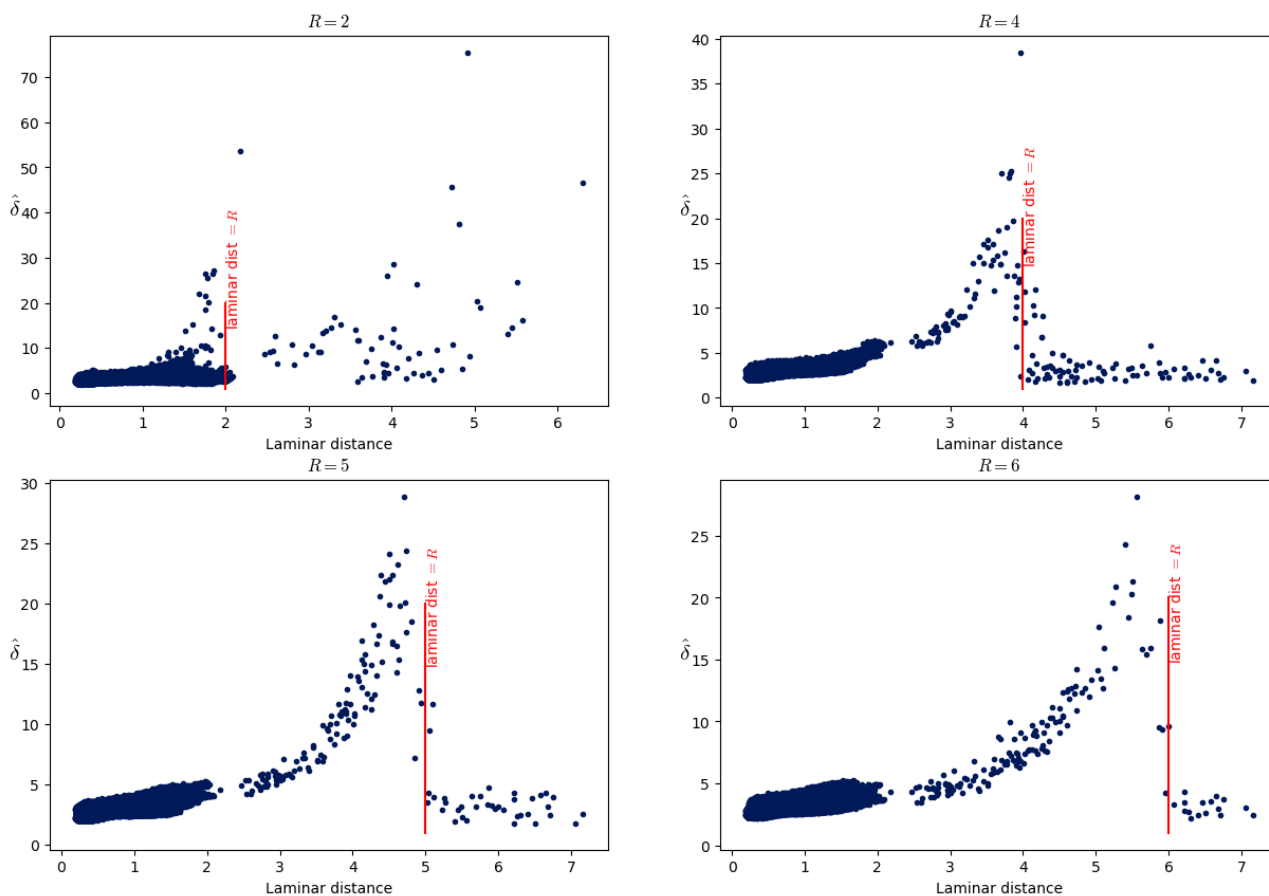
**Figure B2.** Same as Fig. 11 but for the Lorenz 96 system with $n = 12$ and $F = 4.4$ ($10^5$ points in the trajectory). The vertical red lines marks the value of the laminar distance which is equal to the radius $R$.

The time resolution is 5 minutes and we used 6 years of product. A few images are missing in the dataset, which has in total 630 008 radar images. The images are 700x700, with each pixel representing a square of 1kmx1km.

As a complement to Fig. 19, Fig. C1 is a 2D histogram of the mean dimension against the CRR. 5000 computation images were used (instead of 2000 in Section 4.2) in order to have a more reliable histogram.

*Author contributions.* MB and SV designed the work done. MB made the computations and wrote the text. SV helped with discussions about the results and the proofreading of the text.

*Competing interests.* Stéphane Vannitsem is a member of the editorial board of Nonlinear Processes in Geophysics.
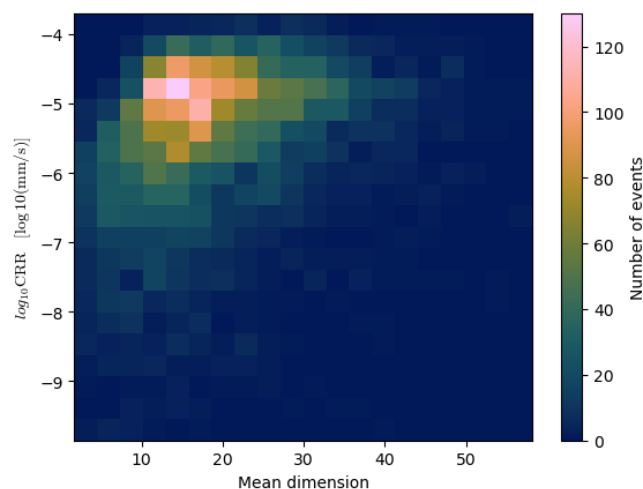
**Figure C1.** 2D histogram of the repartition of the mean dimension for 5000 computation images with the associated CRR.

# References

Abarbanel, H. D. I.: Analysis of Observed Chaotic Data, pp. 69–93, Springer New York, New York, NY, ISBN 978-1-4612-0763-4, https://doi.org/10.1007/978-1-4612-0763-4_5, 1996.

Bac, J. and Zinovyev, A. Y.: Local intrinsic dimensionality estimators based on concentration of measure, 2020 International Joint Conference on Neural Networks (IJCNN), pp. 1–8, https://api.semanticscholar.org/CorpusID:211003705, 2020.

Beirlant, J., Goegebeur, Y., Segers, J., Teugels, J., De Waal, D., and Ferro, C.: Statistics of Extremes: Theory and Applications, Wiley Series in Probability and Statistics, Wiley, ISBN 9780471976479, https://books.google.be/books?id=GtIYLAlTcKEC, 2004.

Berenguer, M., Sempere-Torres, D., and Pegram, G. G.: SBMcast – An ensemble nowcasting technique to assess the uncertainty in rainfall forecasts by Lagrangian extrapolation, Journal of Hydrology, 404, 226–240, https://doi.org/https://doi.org/10.1016/j.jhydrol.2011.04.033, 2011.

Bowler, N., Pierce, C., and Seed, A.: STEPS: A probabilistic precipitation forecasting scheme which merges an extrapolation nowcast with downscaled NWP, Quarterly Journal of the Royal Meteorological Society, 132, 2127 – 2155, https://doi.org/10.1256/qj.04.100, 2007.

Caby, T.: Extreme value theory for dynamical systems, with applications in climate and neuroscience, Theses, Université de Toulon ; Università degli studi dell' Insubria (Come, Italie). Facolta' scienze matematiche, fisiche e naturali, https://theses.hal.science/tel-02473235, 2019.

Camastra, F. and Staiano, A.: Intrinsic dimension estimation: Advances and open problems, Information Sciences, 328, 26–41, https://doi.org/https://doi.org/10.1016/j.ins.2015.08.029, 2016.

Datseris, G., Kottlarz, I., Braun, A. P., and Parlitz, U.: Estimating fractal dimensions: A comparative review and open source implementations, Chaos: An Interdisciplinary Journal of Nonlinear Science, 33, https://doi.org/10.1063/5.0160394, 2023.

De Luca, P., Messori, G., Pons, F. M. E., and Faranda, D.: Dynamical systems theory sheds new light on compound climate extremes in Europe and Eastern North America, Quarterly Journal of the Royal Meteorological Society, 146, 1636–1650, https://doi.org/https://doi.org/10.1002/qj.3757, 2020.

Eckmann, J.-P. and Ruelle, D.: Fundamental limitations for estimating dimensions and Lyapunov exponents in dynamical systems, Physica D: Nonlinear Phenomena, 56, 185–187, https://doi.org/https://doi.org/10.1016/0167-2789(92)90023-G, 1992.

Elaskar, S. and Rio, E.: New Advances on Chaotic Intermittency and its Applications, ISBN 978-3-319-47837-1, https://doi.org/10.1007/978-3-319-47837-1, 2017.

Erba, V., Gherardi, M., and Rotondo, P.: Intrinsic dimension estimation for locally undersampled data, Scientific Reports, 9, https://doi.org/10.1038/s41598-019-53549-9, 2019.

Falk, M., Hüsler, J., and Reiss, R.: Laws of Small Numbers: Extremes and Rare Events, Springer Basel, ISBN 9783034800099, 2010.

Faranda, D., Lucarini, V., Turchetti, G., and Vaienti, S.: Extreme value theory for singular measures, Chaos: An Interdisciplinary Journal of Nonlinear Science, 22, 023 135, https://doi.org/10.1063/1.4718935, 2012.

Faranda, D., Messori, G., and Yiou, P.: Dynamical proxies of North Atlantic predictability and extremes, Scientific Reports, https://doi.org/10.1038/srep41278, 2017.

Faranda, D., Messori, G., and Vannitsem, S.: Attractor dimension of time-averaged climate observables: insights from a low-order ocean-atmosphere model, Tellus A: Dynamic Meteorology and Oceanography, https://doi.org/10.1080/16000870.2018.1554413, 2019.

Faranda, D., Bourdin, S., Ginesta, M., Krouma, M., Noyelle, R., Pons, F., Yiou, P., and Messori, G.: A climate-change attribution retrospective of some impactful weather extremes of 2021, Weather and Climate Dynamics, 3, 1311–1340, https://doi.org/10.5194/wcd-3-1311-2022, 2022.

705

Faranda, D., Pascale, S., and Bulut, B.: Persistent anticyclonic conditions and climate change exacerbated the exceptional 2022 European-Mediterranean drought, Environmental Research Letters, 18, 034 030, https://doi.org/10.1088/1748-9326/acbc37, 2023.

Foresti, L., Puigdomènech Treserras, B., Nerini, D., Atencia, A., Gabella, M., Sideris, I. V., Germann, U., and Zawadzki, I.: A quest for precipitation attractors in weather radar archives, Nonlinear Processes in Geophysics, 31, 259–286, https://doi.org/10.5194/npg-31-259-2024, 2024.

710

Germann, U. and Zawadzki, I.: Scale Dependence of the Predictability of Precipitation from Continental Radar Images. Part II: Probability Forecasts, Journal of Applied Meteorology, 43, 74 – 89, https://doi.org/10.1175/1520-0450(2004)043<0074:SDOTPO>2.0.CO;2, 2004.

Germann, U., Zawadzki, I., and Turner, B.: Predictability of Precipitation from Continental Radar Images. Part IV: Limits to Prediction, Journal of the Atmospheric Sciences, 63, 2092 – 2108, https://doi.org/10.1175/JAS3735.1, 2006.

715 Golay, J. and Kanevski, M. F.: A new estimator of intrinsic dimension based on the multipoint Morisita index, Pattern Recognit., 48, 4070–4081, https://api.semanticscholar.org/CorpusID:31779757, 2014.

Goudenhoofdt, E. and Delobbe, L.: Generation and Verification of Rainfall Estimates from 10-Yr Volumetric Weather Radar Measurements, Journal of Hydrometeorology, 17, 1223 – 1242, https://doi.org/10.1175/JHM-D-15-0166.1, 2016.

Grassberger, P. and Procaccia, I.: Measuring the strangeness of strange attractors, Physica D: Nonlinear Phenomena, 9, 189–208,

720 https://doi.org/https://doi.org/10.1016/0167-2789(83)90298-1, 1983.

James, F. E.: Statistical Methods in Experimental Physics; 2nd ed., World Scientific, Singapore, 2006.

Journée, M., Goudenhoofdt, E., Vannitsem, S., and Delobbe, L.: Quantitative rainfall analysis of the 2021 mid-July flood event in Belgium, Hydrology and Earth System Sciences, 27, 3169–3189, https://doi.org/10.5194/hess-27-3169-2023, 2023.

Little, A. V., Maggioni, M., and Rosasco, L.: Multiscale geometric methods for data sets I: Multiscale SVD, noise and curvature, Applied

725 and Computational Harmonic Analysis, 43, 504–567, https://doi.org/https://doi.org/10.1016/j.acha.2015.09.009, 2017.

Lorenz, E. N.: Deterministic Nonperiodic Flow., Journal of the Atmospheric Sciences, 20, 130–148, https://doi.org/10.1175/1520-0469(1963)020<0130:DNF>2.0.CO;2, 1963.

Lorenz, E. N.: Predictability: A problem partly solved, in: Proc. Seminar on predictability, vol. 1, Reading, 1996.

Lovejoy, S. and Schertzer, D.: The Weather and Climate: Emergent Laws and Multifractal Cascades, Cambridge University Press, 2013.

730 Lucarini, V., Faranda, D., Moreira Freitas, A. C., Freitas, J. M., Mark, H., Tobias, K., Nicol, M., Todd, M., and Vaienti, S.: Extremes and Recurrence in Dynamical Systems, Pure and Applied Mathematics: A Wiley Series of Texts, Monographs and Tracts, Wiley Interscience, https://hal.science/hal-02886423, 2016.

Ott, E.: Chaos in Dynamical Systems, Cambridge University Press, 2 edn., 2002.

Perinelli, A., Iuppa, R., and Ricci, L.: Estimating the correlation dimension of a fractal on a sphere, Chaos, Solitons & Fractals, 173, 113 632,

735 https://doi.org/https://doi.org/10.1016/j.chaos.2023.113632, 2023.

Pesin, Y.: Dimension Theory in Dynamical Systems: Contemporary Views and Applications, Chicago Lectures in Mathematics, University of Chicago Press, ISBN 9780226662213, 1997.

Pierce, C., Seed, A., Ballard, S., Simonin, D., and Li, Z.: Nowcasting, in: Doppler Radar Observations, edited by Bech, J. and Chau, J. L., chap. 4, IntechOpen, Rijeka, https://doi.org/10.5772/39054, 2012.

740 Pomeau, Y. and Manneville, P.: Intermittent transition to turbulence in dissipative dynamical systems, Communications in Mathematical Physics, 74, https://doi.org/10.1007/BF01197757, 1980.

Pons, F. M. E., Messori, G., Alvarez-Castro, M. C., and Faranda, D.: Sampling hyperspheres via extreme value theory: implications for measuring attractor dimensions, Journal of Statistical Physics, https://doi.org/10.1007/s10955-020-02573-5, 2020.

Pons, F. M. E., Messori, G., and Faranda, D.: Statistical performance of local attractor dimension estimators in non-Axiom A dynamical
745 systems, Chaos: An Interdisciplinary Journal of Nonlinear Science, 33, 073 143, https://doi.org/10.1063/5.0152370, 2023.

Pulkkinen, S., Chandrasekar, V., and Harri, A.-M.: Stochastic Spectral Method for Radar-Based Probabilistic Precipitation Nowcasting, Journal of Atmospheric and Oceanic Technology, 36, 971 – 985, https://doi.org/10.1175/JTECH-D-18-0242.1, 2019a.

Pulkkinen, S., Nerini, D., Pérez Hortal, A. A., Velasco-Forero, C., Seed, A., Germann, U., and Foresti, L.: Pysteps: an open-source Python library for probabilistic precipitation nowcasting (v1.0), Geoscientific Model Development, 12, 4185–4219, https://doi.org/10.5194/gmd-
750 12-4185-2019, 2019b.

Russell, D. A., Hanson, J. D., and Ott, E.: Dimension of Strange Attractors, Phys. Rev. Lett., 45, 1175–1178, https://doi.org/10.1103/PhysRevLett.45.1175, 1980.

Schuster, H. and Just, W.: Deterministic Chaos: An Introduction, Wiley, ISBN 9783527606412, 2006.

Scott, D.: Multivariate Density Estimation: Theory, Practice, and Visualization, Wiley Series in Probability and Statistics, Wiley, ISBN
755 9780471697558, 2015.

Seed, A. W.: A Dynamic and Spatial Scaling Approach to Advection Forecasting, Journal of Applied Meteorology, 42, 381 – 388, https://doi.org/10.1175/1520-0450(2003)042<0381:ADASSA>2.0.CO;2, 2003.

Sparrow, C.: The Lorenz Equations: Bifurcations, Chaos, and Strange Attractors, Applied Mathematical Sciences, Springer New York, ISBN 9781461257677, 1982.

760 Sterk, A. and van Kekem, D.: Predictability of Extreme Waves in the Lorenz-96 Model Near Intermittency and Quasi-Periodicity, Complexity, 2017, 1–14, https://doi.org/10.1155/2017/9419024, 2017.

Takens, F.: On the numerical determination of the dimension of an attractor, in: Dynamical Systems and Bifurcations, edited by Braaksma, B. L. J., Broer, H. W., and Takens, F., pp. 99–106, Springer Berlin Heidelberg, Berlin, Heidelberg, ISBN 978-3-540-39411-2, 1985.

Theiler, J.: Spurious dimension from correlation algorithms applied to limited time-series data, Phys. Rev. A, 34, 2427–2432,
765 https://doi.org/10.1103/PhysRevA.34.2427, 1986.

Theiler, J.: Statistical precision of dimension estimators, Phys. Rev. A, 41, 3038–3051, https://doi.org/10.1103/PhysRevA.41.3038, 1990.

van Kekem, D. L. and Sterk, A. E.: Travelling waves and their bifurcations in the Lorenz-96 model, Physica D: Nonlinear Phenomena, 367, 38–60, https://doi.org/https://doi.org/10.1016/j.physd.2017.11.008, 2018.

Veneziano, D., Langousis, A., and Furcolo, P.: Multifractality and rainfall extremes: A review, Water Resources Research, 42,
770 https://doi.org/https://doi.org/10.1029/2005WR004716, 2006.

Zawadzki, I., Morneau, J., and Laprise, R.: Predictability of Precipitation Patterns: An Operational Approach, Journal of Applied Meteorology and Climatology, 33, 1562 – 1571, https://doi.org/10.1175/1520-0450(1994)033<1562:POPPAO>2.0.CO;2, 1994.